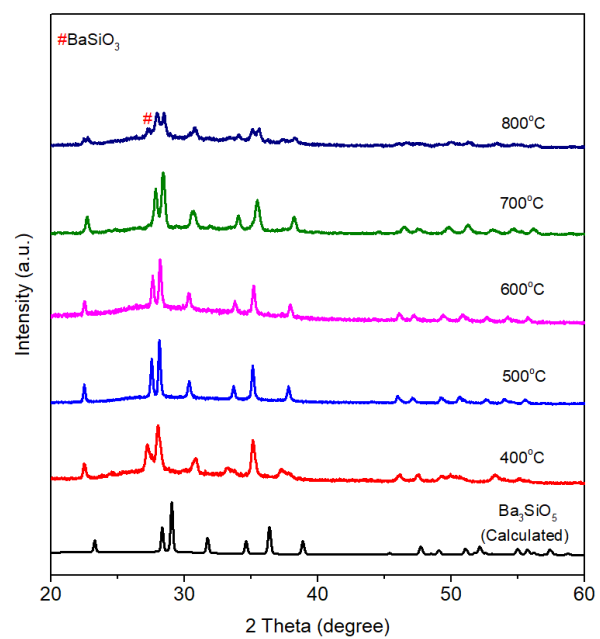


Anion vacancies activate N_2 to ammonia on Ba–Si orthosilicate oxynitride-hydride

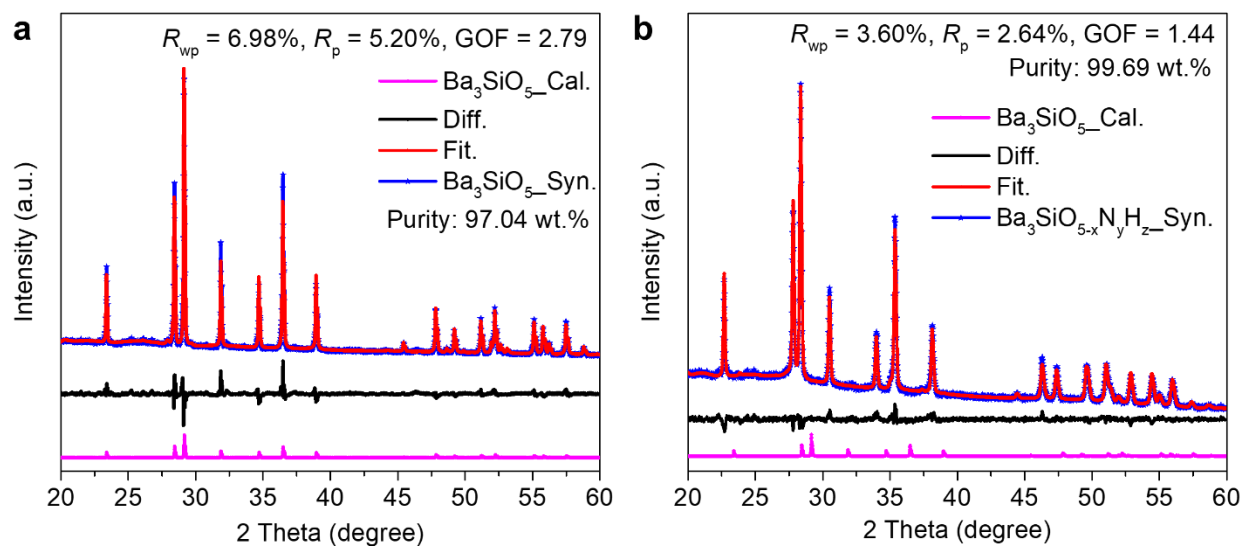
In the format provided by the
authors and unedited

Table of contents

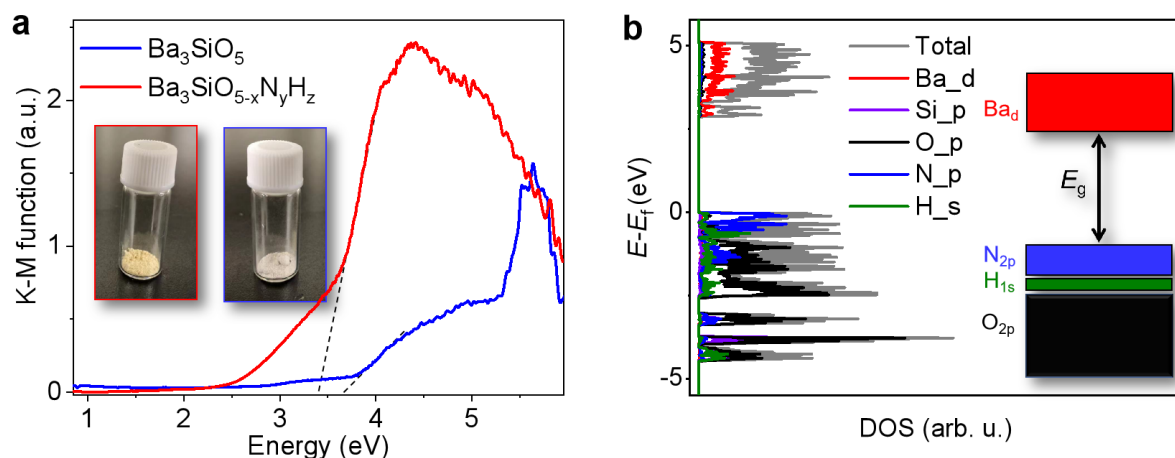
1. Supplementary Figs. 1-45	2-46
2. Supplementary Table 1-7	47-53



Supplementary Fig. 1. XRD patterns of $\text{Ba}_3\text{SiO}_{5-x}\text{N}_y\text{H}_z$ synthesized at various temperatures. The pure tetragonal Ba_3SiO_5 phase can be obtained at $400\text{--}700^\circ\text{C}$.

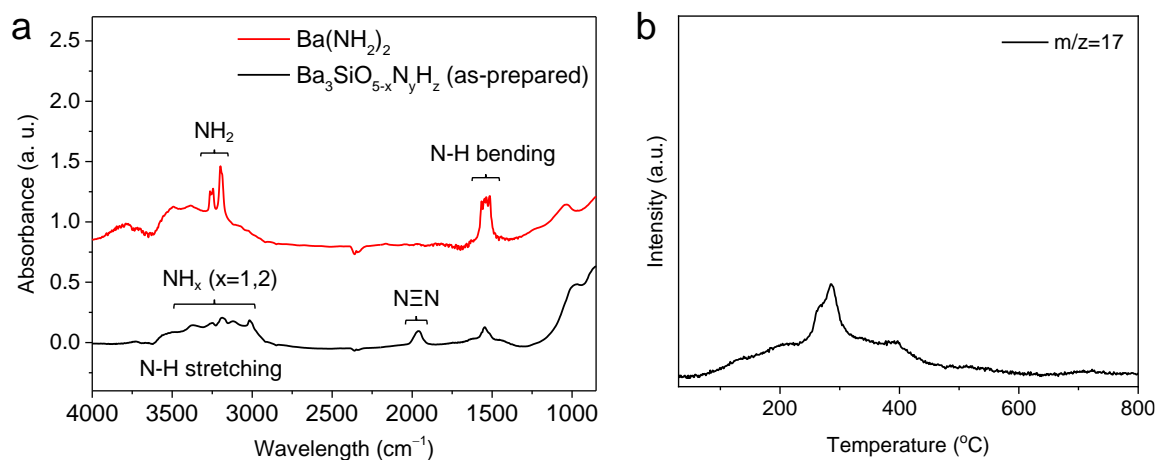


Supplementary Fig. 2. Experimental XRD patterns of (a) as-synthesized Ba_3SiO_5 and (b) $Ba_3SiO_{5-x}N_yH_z$ (prepared at $600^\circ C$) with Rietveld fitting. Both Ba_3SiO_5 and $Ba_3SiO_{5-x}N_yH_z$ have the same crystal structure (tetragonal symmetry, $I4/mcm$).



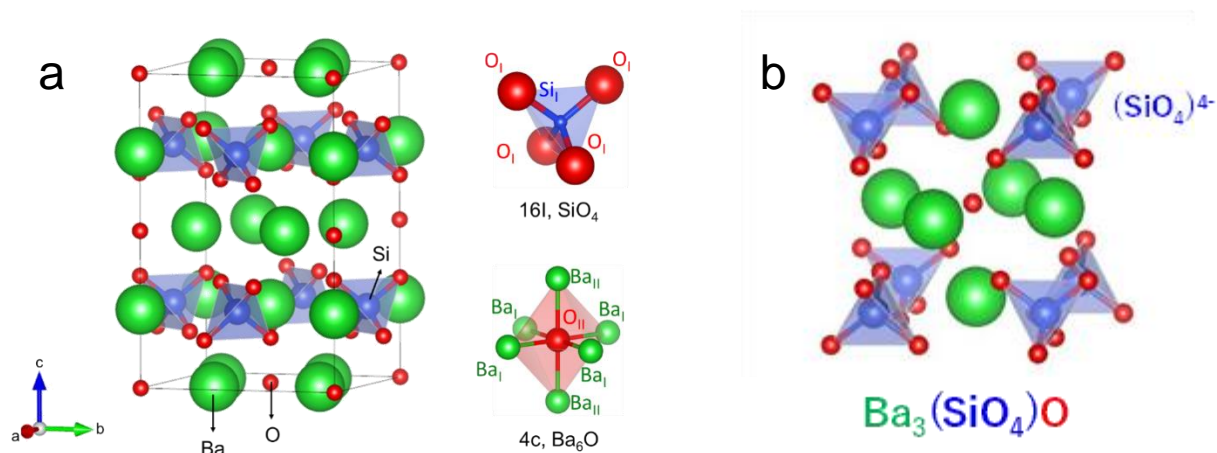
Supplementary Fig. 3. (a) Diffuse reflectance spectra for $\text{Ba}_3\text{SiO}_{5-x}\text{N}_y\text{H}_z$ and Ba_3SiO_5 . Inset: photograph of the $\text{Ba}_3\text{SiO}_{5-x}\text{N}_y\text{H}_z$ and Ba_3SiO_5 powder. (b) Projected DOSs of calculated $\text{Ba}_3\text{SiO}_{2.5}\text{NH}_2$. Inset: band structure of calculated $\text{Ba}_3\text{SiO}_{2.5}\text{NH}_2$.

The white colored Ba_3SiO_5 powder, which was obtained by heating a mixture of BaCO_3 and SiO_2 at 1250 °C in a gasses flow of Ar (95%) and H_2 (5%) for 20 h, has a wide band gap of *ca.* 3.7 eV as determined by the Tauc plot analysis of the diffuse reflectance spectrum (DRS) (Supplementary Fig. 3a). On the other hand, the yellow colored $\text{Ba}_3\text{SiO}_{5-x}\text{N}_y\text{H}_z$ powder has a much narrower band gap of *ca.* 3.4 eV. In $\text{Ba}_3\text{SiO}_{5-x}\text{N}_y\text{H}_z$, broad shoulder absorption was observed below the band gap energies, which is attributed to the presence of V_a . Based on a projected density of states (DOSs) analysis (Supplementary Fig. 3b), the conduction band minimum (CBM) is dominated by Ba_vacant 5d orbitals, and strong hybridization of the N_2p and H_1s orbitals with O_2p orbitals upshifts the valance band maximum (VBM). In particular, the N_2p band occupies above the H_1s and O_2p bands, and thus contributes mostly to the observed band gap narrowing.



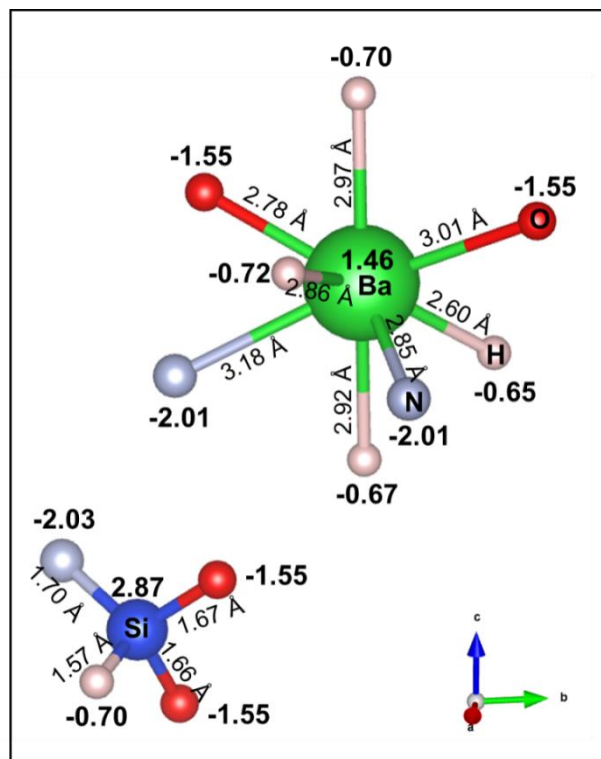
Supplementary Fig. 4. (a) FT-IR spectra of as-prepared Ba₃SiO_{5-x}N_yH_z and barium amide (Ba(NH₂)₂). (b) TPD of NH₃ from as-prepared Ba₃SiO_{5-x}N_yH_z. The NH_x species would be formed on the sample surface during the synthesis of Ba₃SiO_{5-x}N_yH_z.

Both the broad N-H_x (x=1,2) stretching band at around 3200 cm⁻¹ and weak N-H bending vibration at 1543 cm⁻¹ can be observed for as-prepared Ba₃SiO_{5-x}N_yH_z. This IR result agrees well with the results of solid state NMR (Fig. 1b). The amount of NH_x species was estimated to be 0.04 mmol g⁻¹ based on TPD of NH₃ (Supplementary Fig. 4b), which is only around 2.5% that of total lattice N³⁻. These results indicate that most hydrogen species are present as hydridic H in the lattice, but a small amount of NH species is also formed on the Ba₃SiO_{5-x}N_yH_z surface.

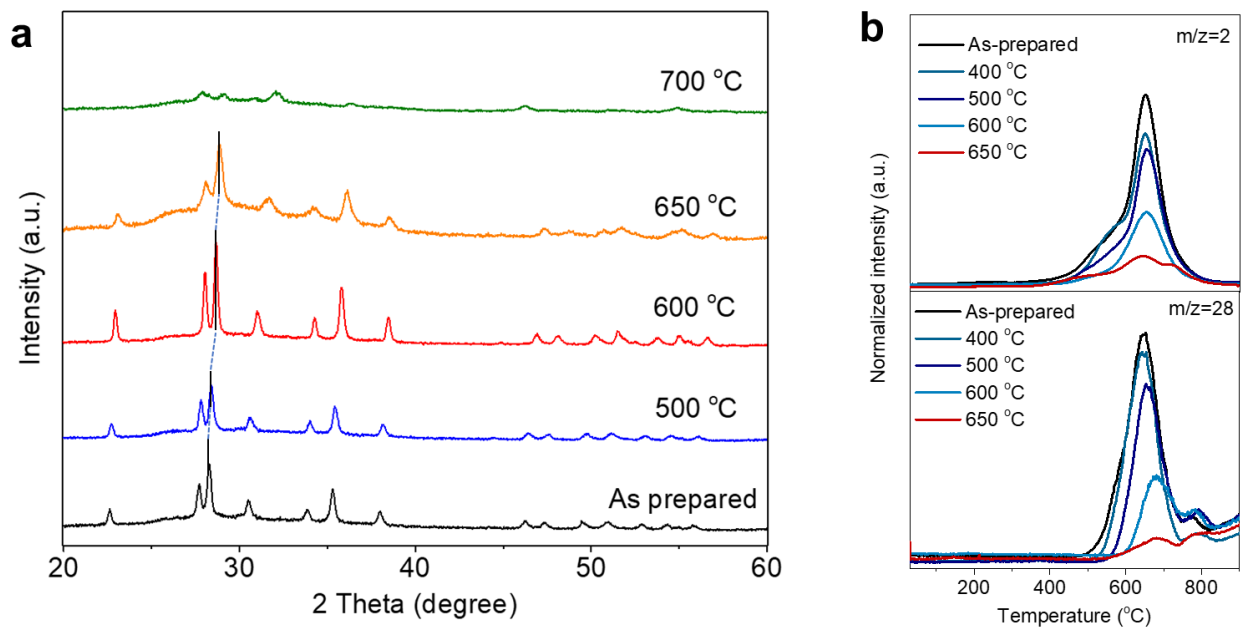


Supplementary Fig. 5. (a) Crystal structure of Ba_3SiO_5 (left). Local structure of SiO_4 and Ba_6O block (right). (b) Antiperovskite-like unit of Ba_3SiO_5

Ba_3SiO_5 can be regarded as A_3BX -type antiperovskite. The oxygen occupies the center of the octahedral site (X) and is coordinated by 6 Ba (A). The large complex anions, $(\text{SiO}_4)^{4-}$, occupy the B sites. The tetragonal Ba_3SiO_5 crystal has two types of oxygen sites, i.e., four O_I sites bonded with one silicon (SiO_4) and one O_II site surrounded by six barium atoms (Ba_6O).

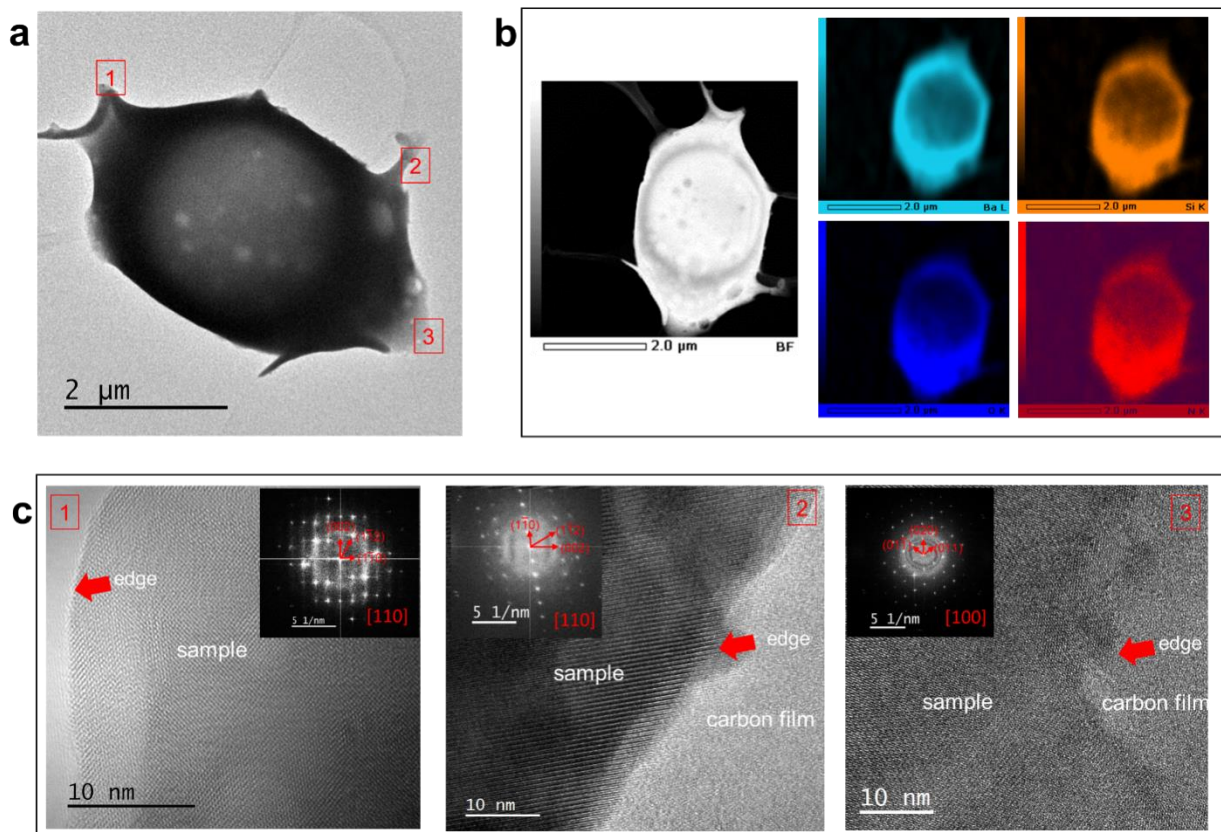


Supplementary Fig. 6. The Ba-H, Si-N, Si-H bond distances of $\text{Ba}_3\text{SiO}_{2.5}\text{N}_{1.0}\text{H}_{2.0}$, as well as the charge of each element determined by DFT calculations.



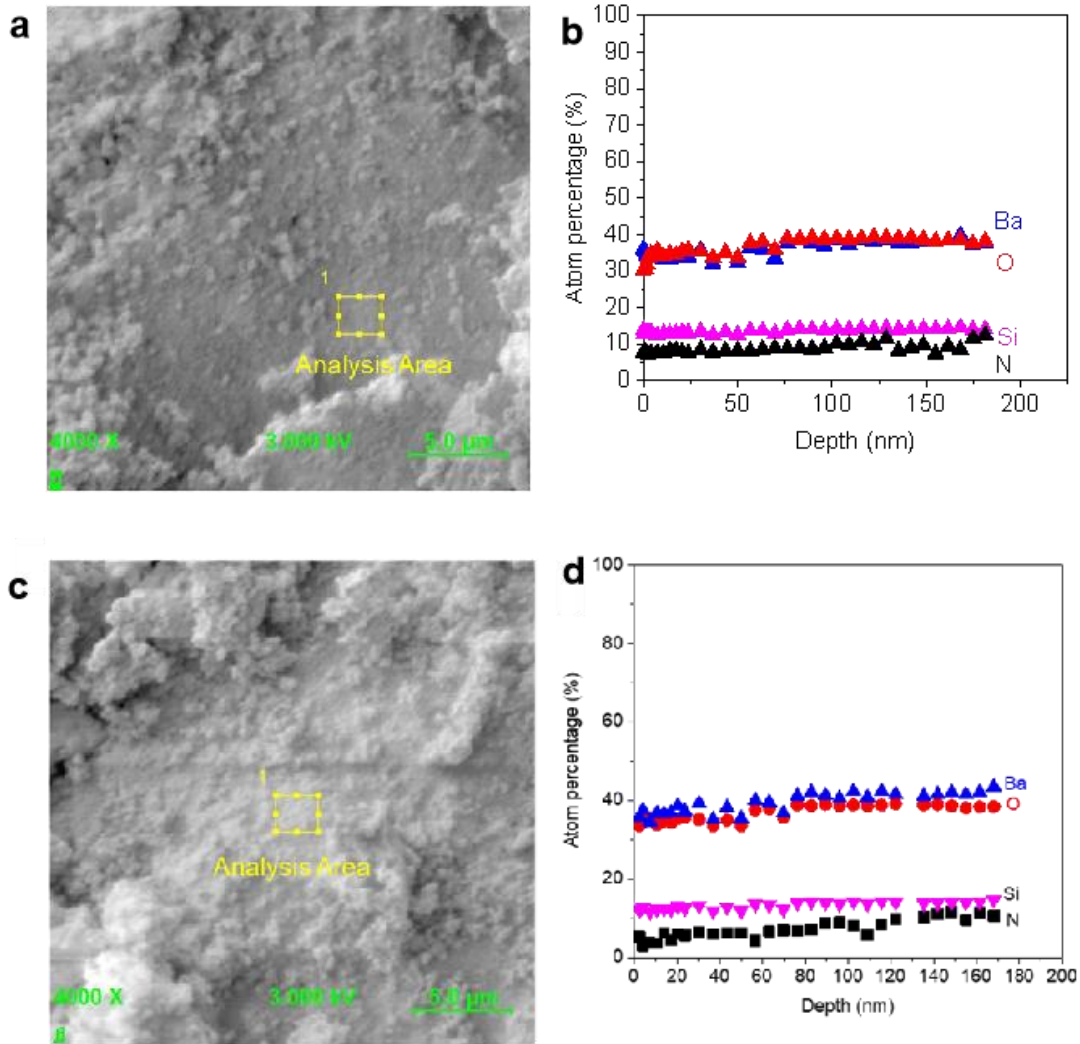
Supplementary Fig. 7. (a) XRD patterns of $\text{Ba}_3\text{SiO}_{5-x}\text{N}_y\text{H}_z$ heated in Ar flow at various temperatures. (b) TPD profiles of $\text{Ba}_3\text{SiO}_{5-x}\text{N}_y\text{H}_z$ before and after heating in Ar at various temperatures.

The tetragonal structure of $\text{Ba}_3\text{SiO}_{5-x}\text{N}_y\text{H}_z$ was preserved up to 650 °C; however, the diffraction peaks shifted to higher angles compared to those of the as-prepared sample as a result of lattice shrinkage induced by the removal of lattice H^- and N^{3-} ions.



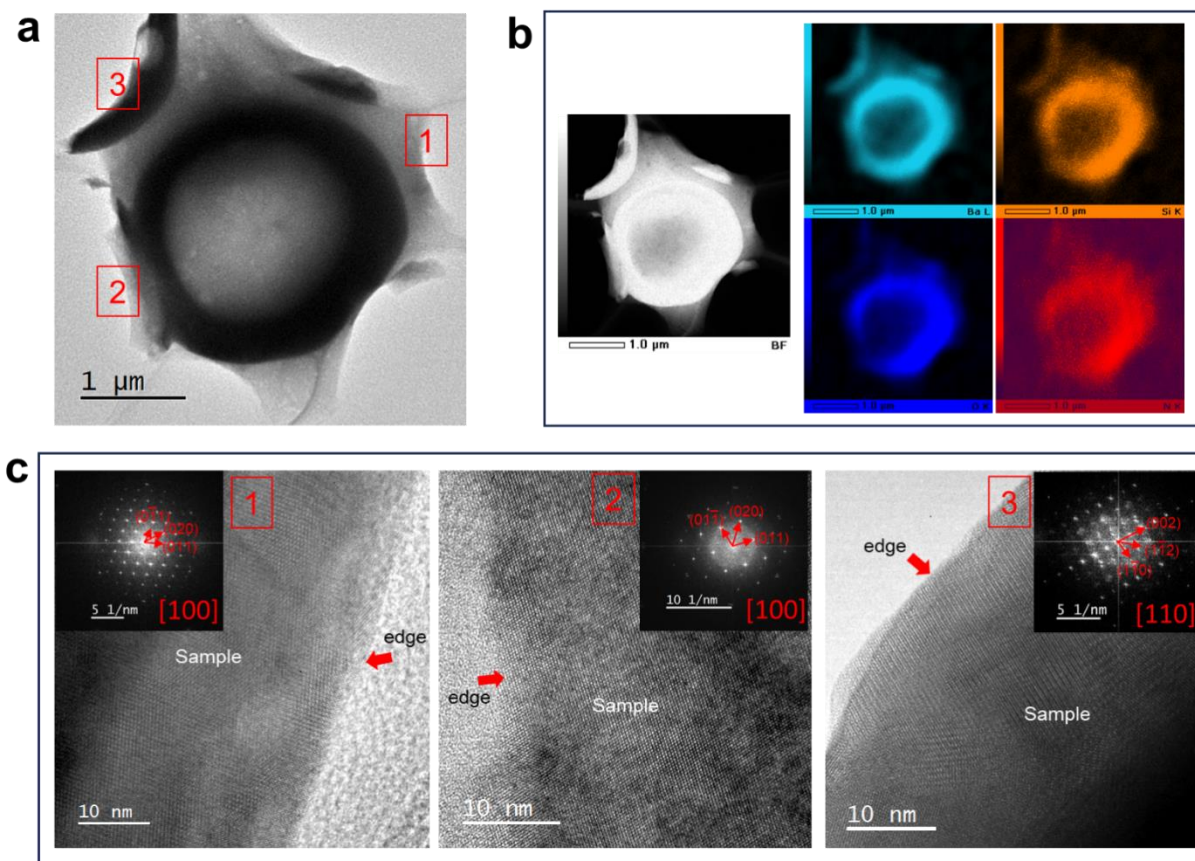
Supplementary Fig. 8. TEM image (a) and HAADF-STEM image with corresponding EDS-mapping (b) of a typical particle of $\text{Ba}_3\text{SiO}_{5-x}\text{N}_y\text{H}_z$ collected after ammonia synthesis. (c) High resolution TEM images and fast Fourier transform (FFT) pattern of $\text{Ba}_3\text{SiO}_{5-x}\text{N}_y\text{H}_z$ focused in each area of Supplementary Fig. 8a.

The lattice fringes can be clearly seen in all regions in Supplementary Fig. 8a. The corresponding FFT pattern along the (110) and (100) axis gives bright spots, indicating that the $\text{Ba}_3\text{SiO}_{5-x}\text{N}_y\text{H}_z$ is well crystallized without any amorphous phase. The FFT pattern agrees well with the diffraction from Ba_3SiO_5 phase (tetragonal symmetry, $I4/mcm$).



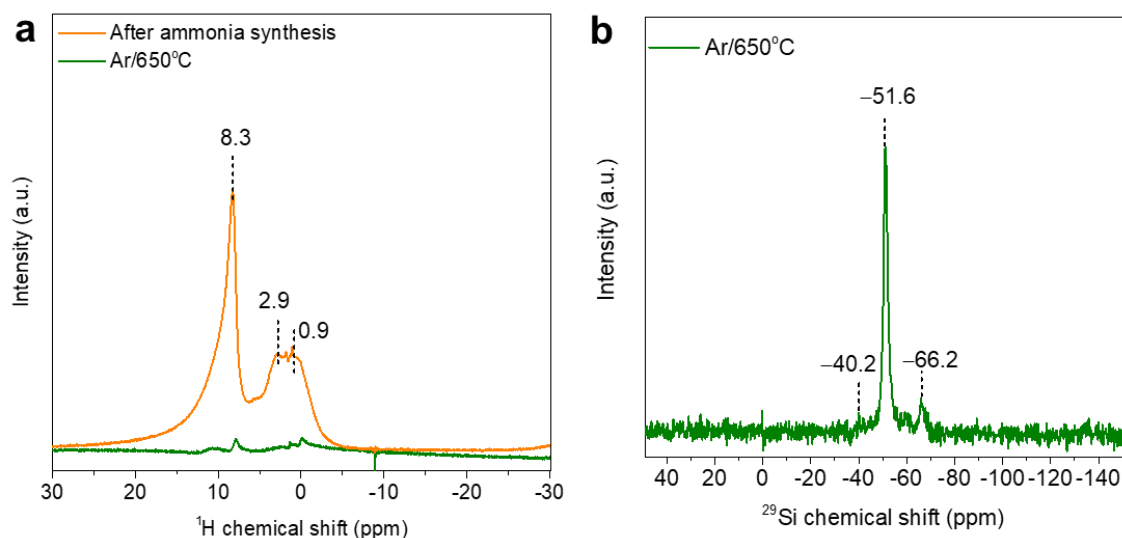
Supplementary Fig. 9. AES depth profile of as-prepared $\text{Ba}_3\text{SiO}_{5-x}\text{N}_y\text{H}_z$ (a,b) and $\text{Ba}_3\text{SiO}_{5-x}\text{N}_y\text{H}_z$ collected after ammonia synthesis (c,d).

Ba, Si, O, and N elements are uniformly distributed from the surface to bulk region and the elemental ratio is well consistent with $\text{Ba}_3\text{SiO}_{2.87}\text{N}_{0.80}\text{H}_{1.86}$ determined by other elemental analyses. The contribution of impurity phase to the catalytic performance of $\text{Ba}_3\text{SiO}_{5-x}\text{N}_y\text{H}_z$ can be ruled out.



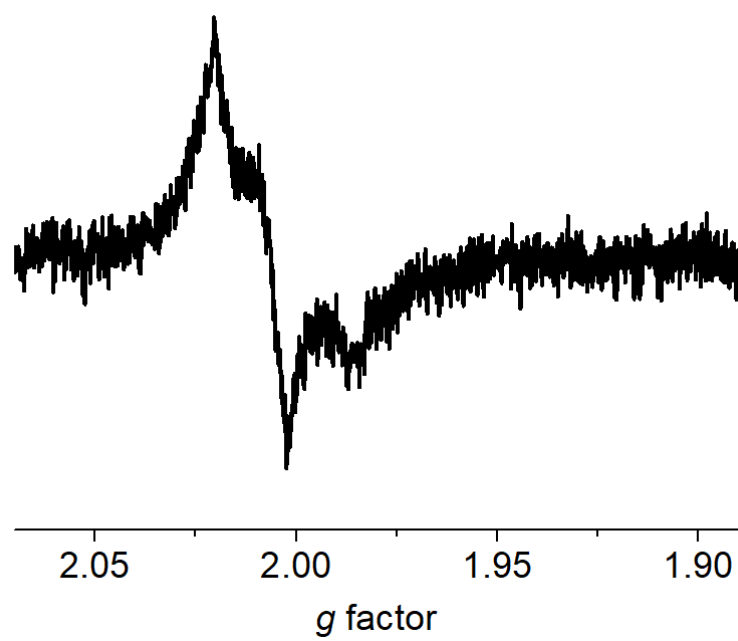
Supplementary Fig. 10. TEM image (a) and HAADF-STEM image with corresponding EDS-mapping (b) of a typical particle of $\text{Ba}_3\text{SiO}_{5-x}\text{N}_y\text{H}_z$ collected after heated in Ar flow at 650°C for 2 h. (c) High resolution TEM images and FFT pattern of the same sample focused in each area of Supplementary Fig. 10a.

The lattice fringes and FFT spot pattern can be clearly seen in all regions in Supplementary Fig. 10c, indicating that the crystal structure of $\text{Ba}_3\text{SiO}_{5-x}\text{N}_y\text{H}_z$ is maintained after Ar heat treatment without formation of any impurity phase.

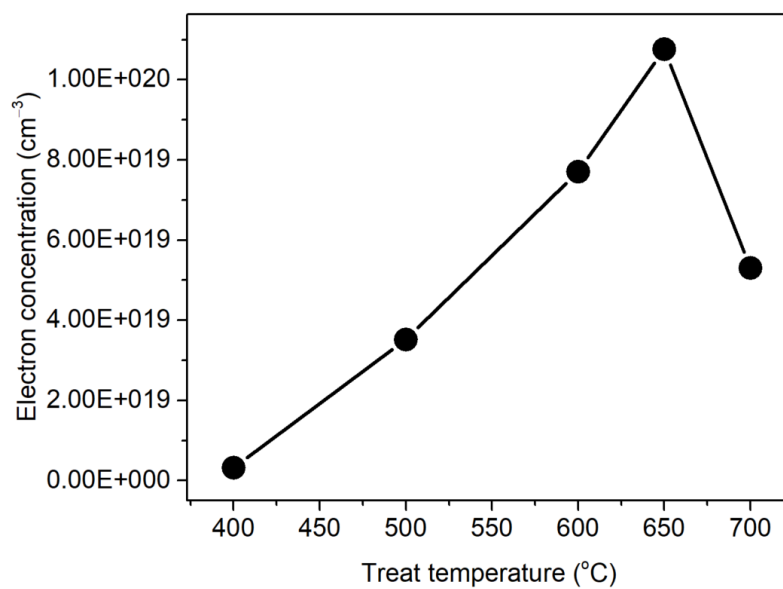


Supplementary Fig. 11. (a) Solid-state ^1H MAS NMR of $\text{Ba}_3\text{SiO}_{5-x}\text{N}_y\text{H}_z$ Ar/650°C and $\text{Ba}_3\text{SiO}_{5-x}\text{N}_y\text{H}_z$ Ar/650°C-used. (b) Solid-state ^{29}Si MAS NMR of $\text{Ba}_3\text{SiO}_{5-x}\text{N}_y\text{H}_z$ Ar/650°C.

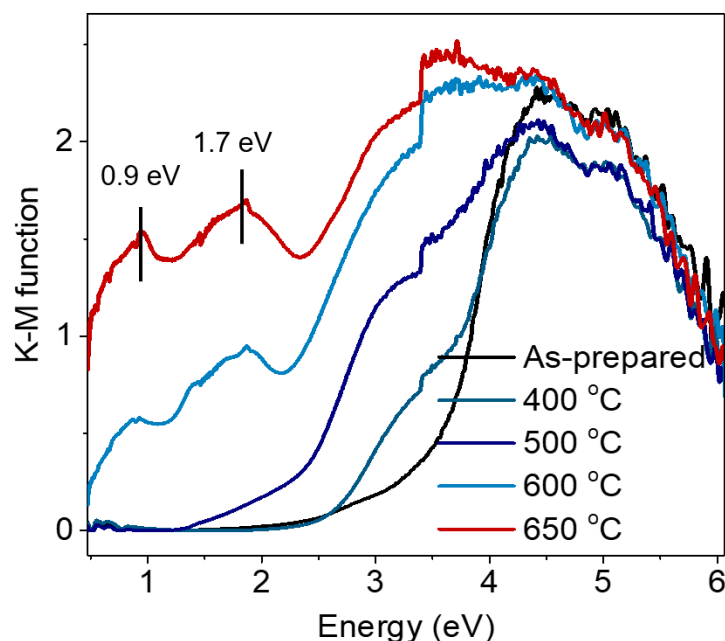
After heat treatment at 650°C in Ar, ^1H -NMR signals almost disappeared, but the signal of hydrides can be regenerated when the sample is exposed in the ammonia synthesis conditions. These results indicate the heat treatment (Ar/650°C) removes most of H^- from the lattice. After heat treatment at 650°C in Ar, the ^{29}Si -NMR signals at around -30 and -40 ppm almost disappeared, but the ^{29}Si -NMR signals at around -66 and -51.6 ppm remained. Therefore, SiO_2NH and SiONH_2 are converted into SiO_xN species. As a conclusion, we can confirm that the heat treatment in Ar at 650°C would remove a large amount of lattice H^- and surface N^{3-} from $\text{Ba}_3\text{SiO}_{5-x}\text{N}_y\text{H}_z$ without decomposition of the crystal structure.



Supplementary Fig. 12. EPR spectra of as-prepared $\text{Ba}_3\text{SiO}_{5-x}\text{N}_y\text{H}_z$ shown in Fig. 1f.

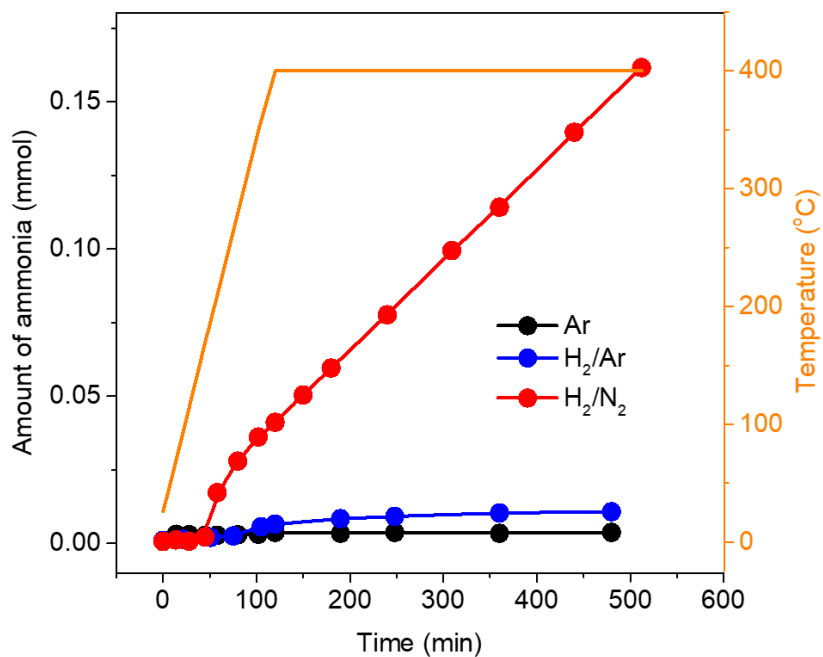


Supplementary Fig. 13. Electron concentration of $\text{Ba}_3\text{SiO}_{5-x}\text{N}_y\text{H}_z$ heated at various temperatures. The electron concentration was determined by the EPR signal using standard $\text{CuSO}_4 \cdot 5\text{H}_2\text{O}$ crystals.



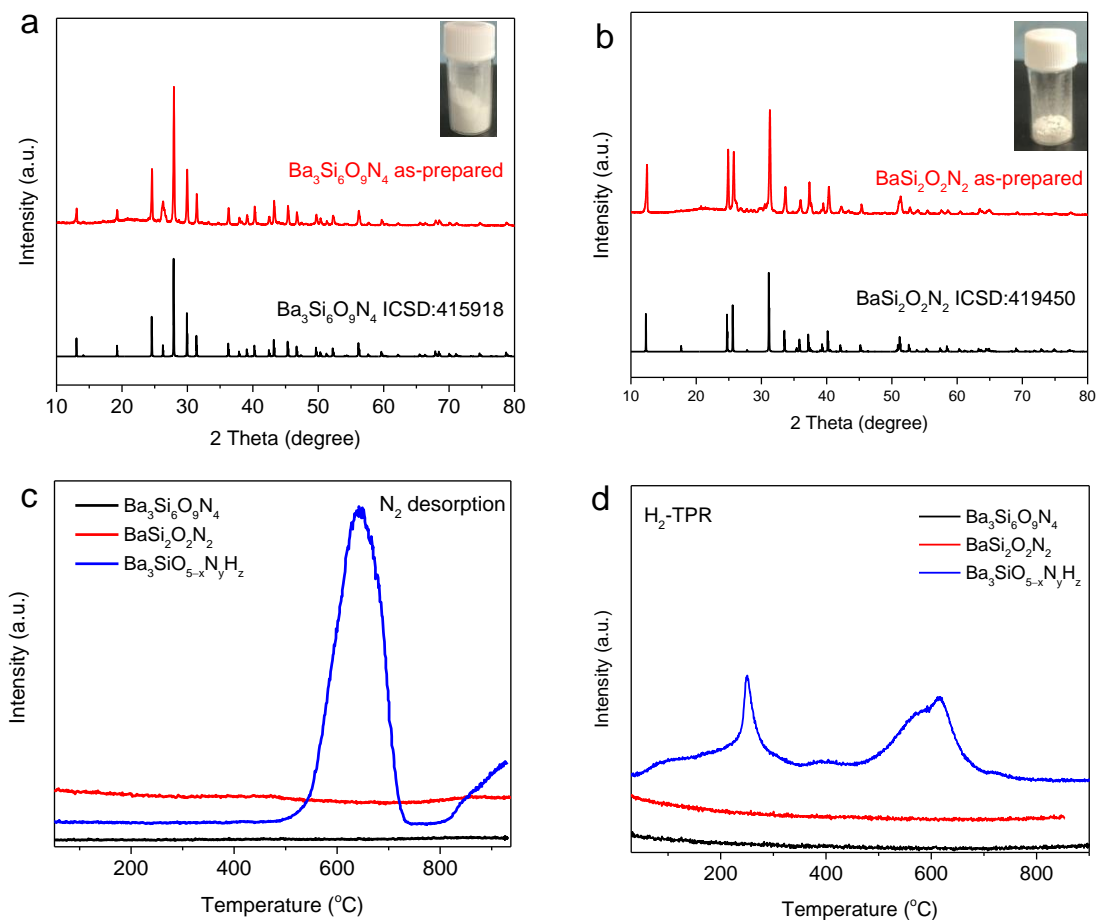
Supplementary Fig. 14. Diffuse reflectance spectra of $\text{Ba}_3\text{SiO}_{5-x}\text{N}_y\text{H}_z$ before and after heating in Ar at various temperatures.

In addition to the band gap absorption of $\text{Ba}_3\text{SiO}_{5-x}\text{N}_y\text{H}_z$ at ca. 3.6 eV, new isolated absorption peaks below 3.6 eV emerged with the increased temperature. In particular, two optical absorption bands centered at around 1.7 and 0.9 eV were observed for the samples heated at above 600°C, which gave rise to a persistent color change from light yellow to dark green (Fig. 1e). These new absorption bands are attributed to the formation of anionic electrons confined at V_a sites, which is analogous to the C12A7 electride¹¹, which was further investigated by EPR analysis (Fig. 1f).

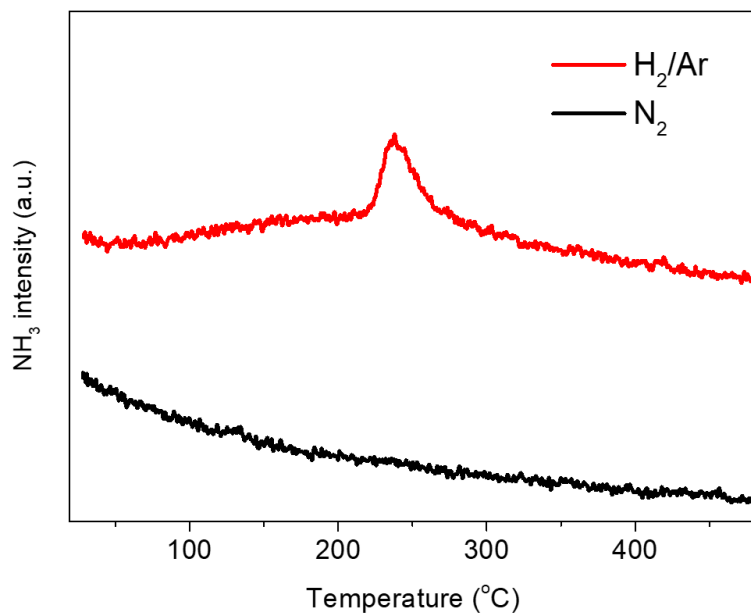


Supplementary Fig. 15. Ammonia formation over $\text{Ba}_3\text{SiO}_{5-x}\text{N}_y\text{H}_z$ under different gas flow at 400°C and 0.9 MPa . The amounts of ammonia produced under Ar and H_2/Ar are 0.004 and 0.011 mmol, respectively, which are lower than the amount of lattice N (0.16 mmol) in $\text{Ba}_3\text{SiO}_{5-x}\text{N}_y\text{H}_z$.

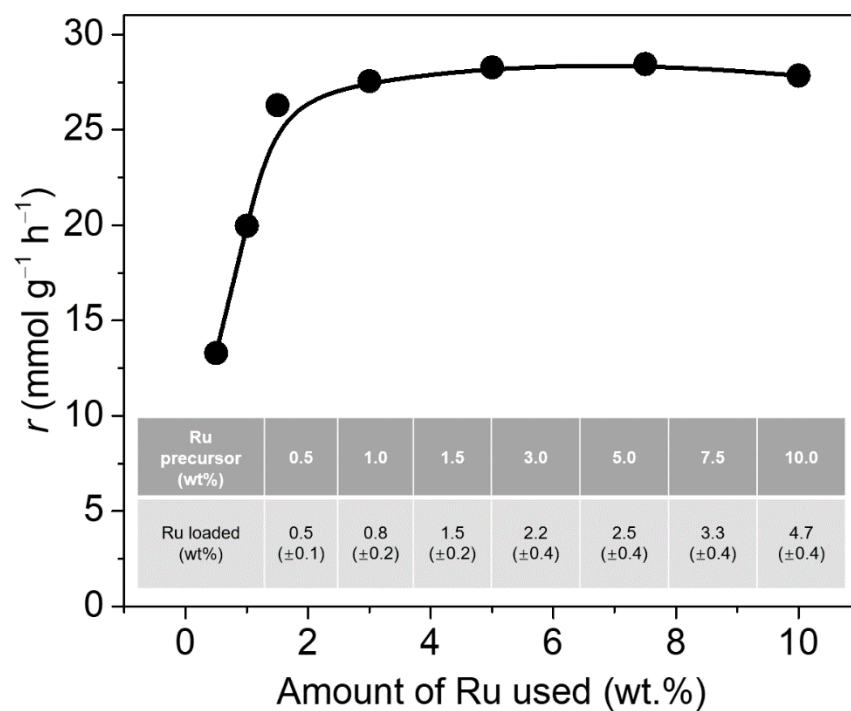
The ammonia formation induced by thermal decomposition of $\text{Ba}_3\text{SiO}_{5-x}\text{N}_y\text{H}_z$ is negligibly low as compared with the catalytic ammonia production.



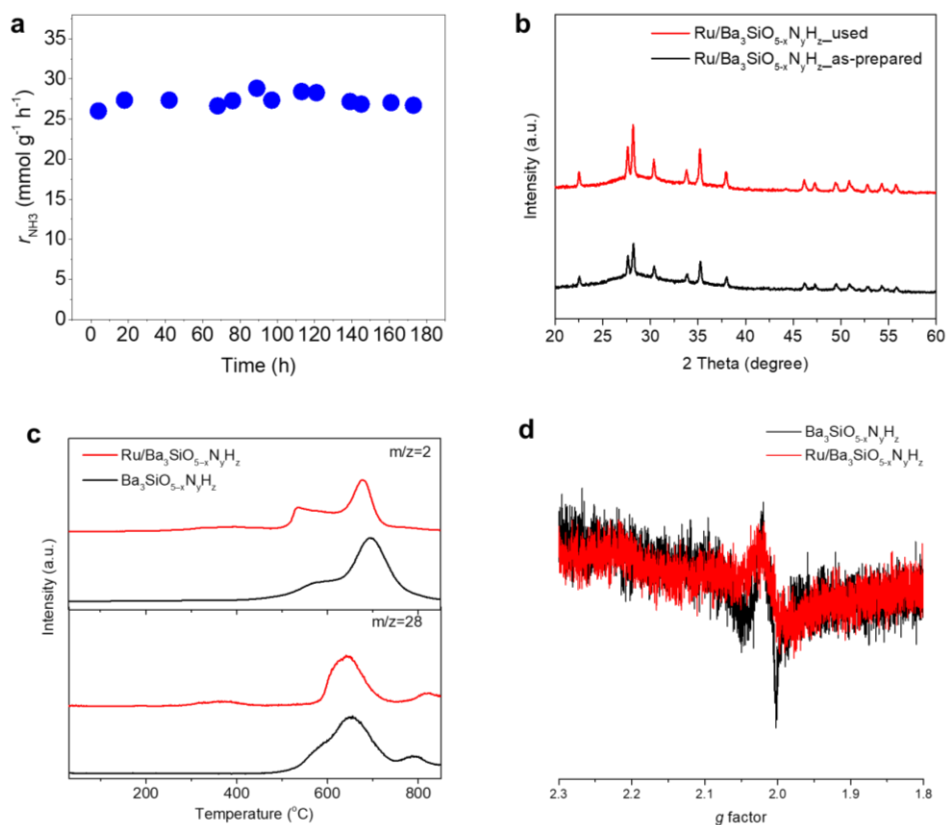
Supplementary Fig. 16. XRD patterns of (a) $\text{Ba}_3\text{Si}_6\text{O}_9\text{N}_4$ and (b) $\text{BaSi}_2\text{O}_2\text{N}_2$ powder prepared by reported procedures. Inset shows the photograph of each sample. (c) TPD of N_2 ($m/z=28$) under Ar atmosphere and (d) NH_3 desorption ($m/z=17$) profiles during H_2 -TPR from $\text{Ba}_3\text{Si}_6\text{O}_9\text{N}_4$ (black line), $\text{BaSi}_2\text{O}_2\text{N}_2$ (red line), and $\text{Ba}_3\text{SiO}_{5-x}\text{N}_y\text{H}_z$ (blue line) in a flow of $\text{H}_2(5\%)/\text{Ar}$.



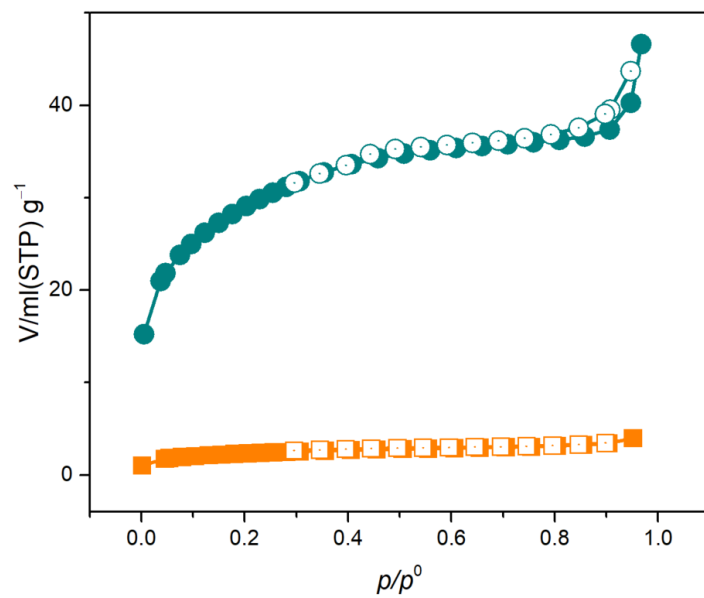
Supplementary Fig. 17. Temperature-programmed NH₃ formation ($m/z=17$) from Ba₃SiO_{5-x}N_yH_z in a flow of pure N₂ and H₂(5%)/Ar (the same result shown in **Supplementary Fig. 16d**, but the temperature region is below 500 °C).



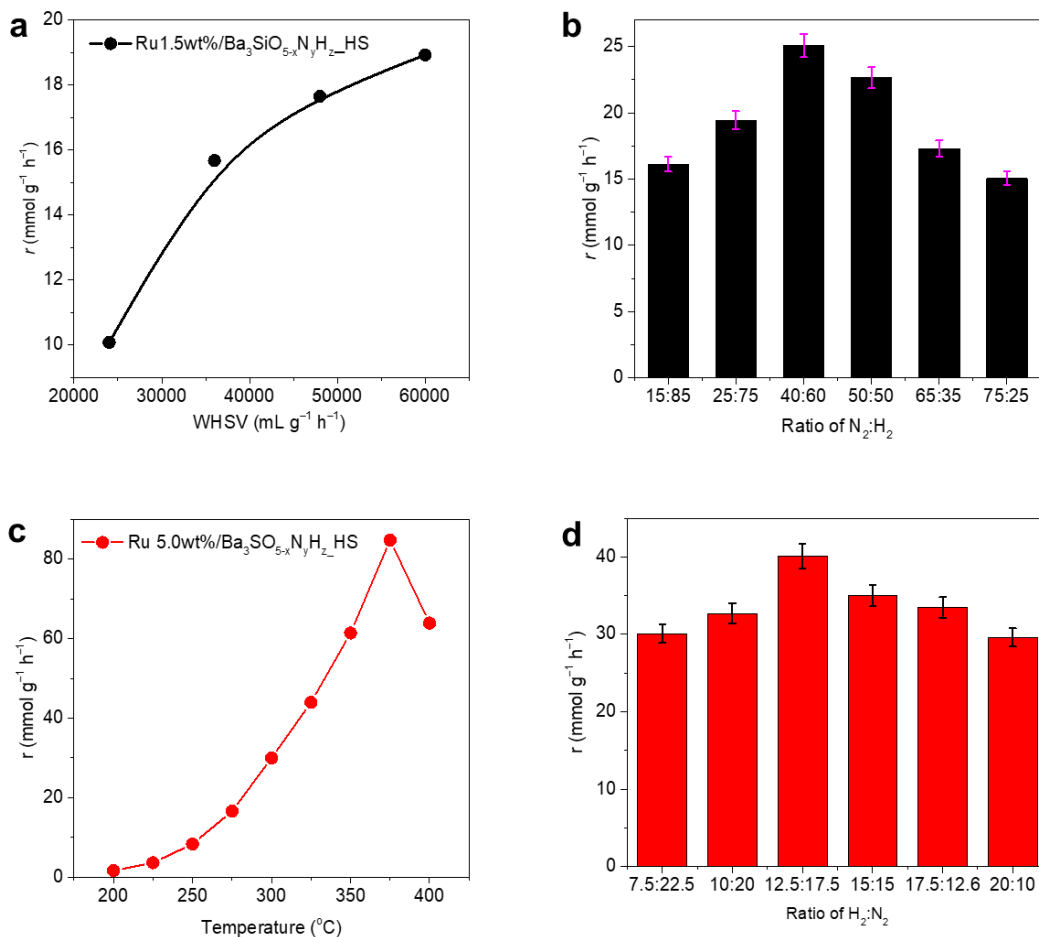
Supplementary Fig. 18. Ammonia synthesis activity of Ru/Ba₃SiO_{5-x}N_yH_z prepared with different amounts of Ru precursors. (Reaction conditions: 0.1 g catalyst, N₂/H₂ = 15:45 mL min⁻¹, 0.9 MPa, 400°C). The inset table shows the actual loading amount of Ru was determined by XRF analysis of the used samples.



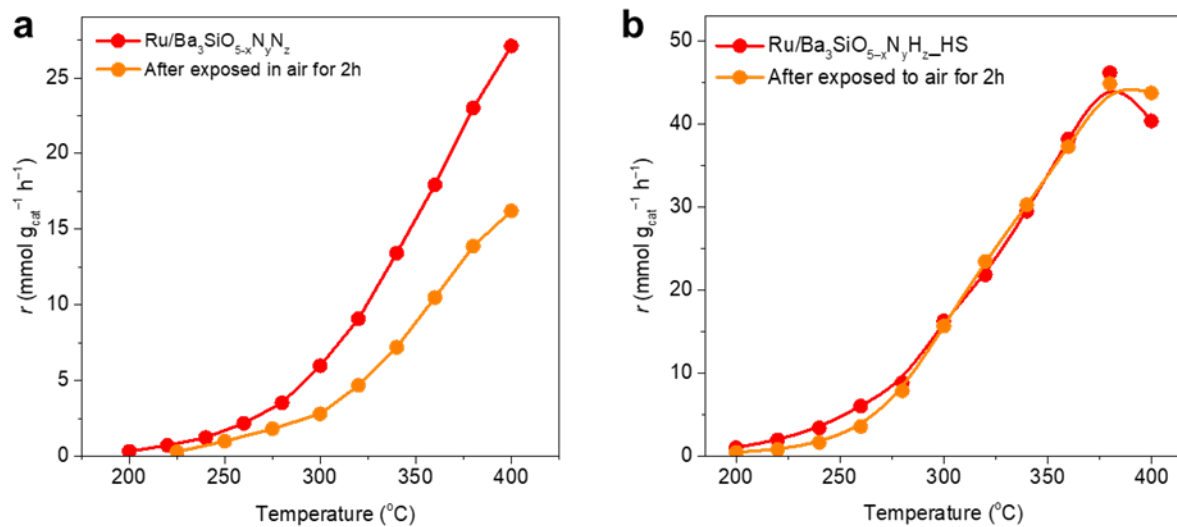
Supplementary Fig. 19. (a) Time courses for ammonia synthesis over Ru(1.5wt.)/Ba₃SiO_{5-x}N_yH_z at 400°C and 0.9 MPa. (b) XRD patterns of as-prepared Ru(1.5wt.)/Ba₃SiO_{5-x}N_yH_z and after ammonia synthesis test. (c) TPD analysis of H₂ and N₂ release from Ba₃SiO_{5-x}N_yH_z and Ru(1.5wt.)/Ba₃SiO_{5-x}N_yH_z (these samples were collected after ammonia synthesis test) under Ar atmosphere. (d) X-band EPR spectra of Ba₃SiO_{5-x}N_yH_z and Ru(1.5wt.)/Ba₃SiO_{5-x}N_yH_z (these samples were collected after ammonia synthesis test).



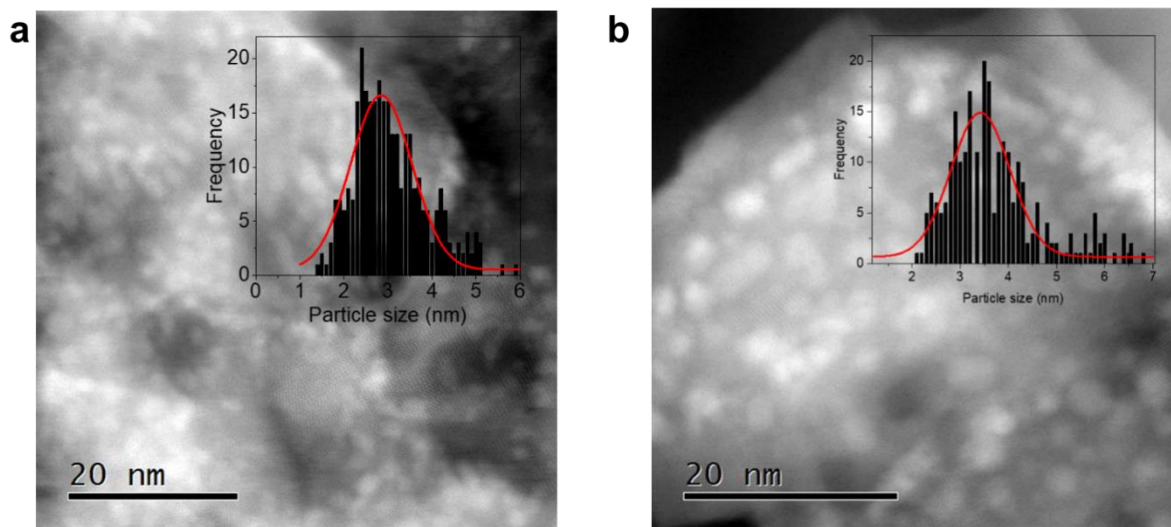
Supplementary Fig. 20. Nitrogen gas adsorption–desorption isotherm of as-prepared $\text{Ba}_3\text{SiO}_{5-x}\text{N}_y\text{H}_z$ (orange curve) and $\text{Ba}_3\text{SiO}_{5-x}\text{N}_y\text{H}_z\text{_{HS}}$ (green curve) powders.



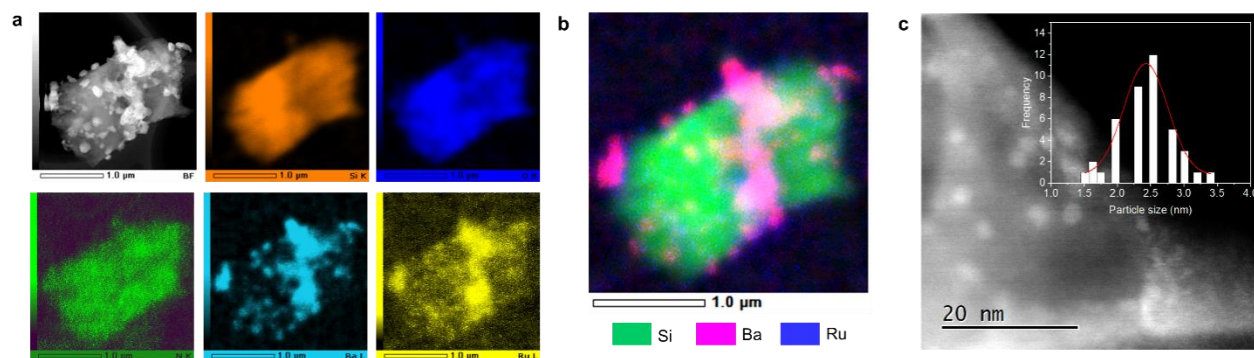
Supplementary Fig. 21. **a**, Ammonia synthesis rates of Ru/Ba₃SiO_{5-x}N_yH_z_HS tested at 300°C and 0.9 MPa under various WHSV (Catalyst: 0.1 g; Temperature: 300°C). **b**, Ammonia synthesis rates of Ru(1.5wt%)/Ba₃SiO_{5-x}N_yH_z_HS tested at 300°C, 0.9 MPa and WHSV of 60000 mL g⁻¹ h⁻¹ with various ratios of N₂ and H₂ (Catalyst: 0.1 g). **c**, Temperature dependence of the ammonia synthesis rate over Ru(5.0wt%)/Ba₃SiO_{5-x}N_yH_z_HS tested at 300°C and 1.0 MPa under a WHSV of 60000 mL g⁻¹ h⁻¹ with H₂:N₂ ratio of 3 (Catalyst: 0.03 g). **d**, Ammonia synthesis rates of Ru(5.0wt%)/Ba₃SiO_{5-x}N_yH_z_HS tested at 300°C, 0.9 MPa and WHSV of 60000 mL g⁻¹ h⁻¹ with various ratios of N₂ and H₂ (Catalyst: 0.03 g). The error range defined as the standard deviation for a set of experimental runs (n = 3) was ±4%.



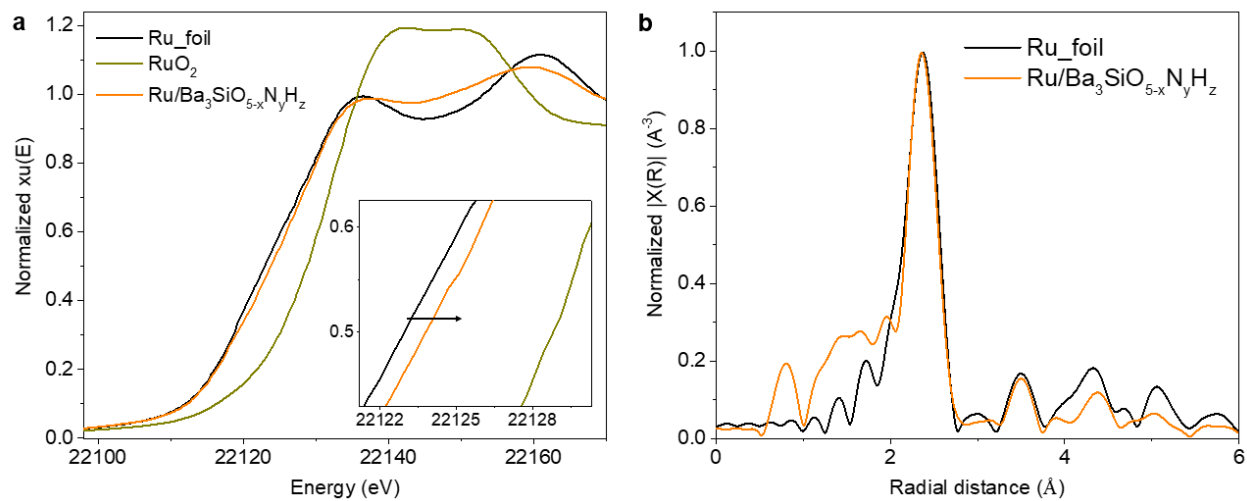
Supplementary Fig. 22. Temperature dependence of the ammonia synthesis rate over (a) $\text{Ru/Ba}_3\text{SiO}_{5-x}\text{N}_y\text{H}_z$ and (b) of $\text{Ru/Ba}_3\text{SiO}_{5-x}\text{N}_y\text{H}_z\text{-HS}$ under a pressure of 0.9 MPa before and after exposed in air for 2 h.



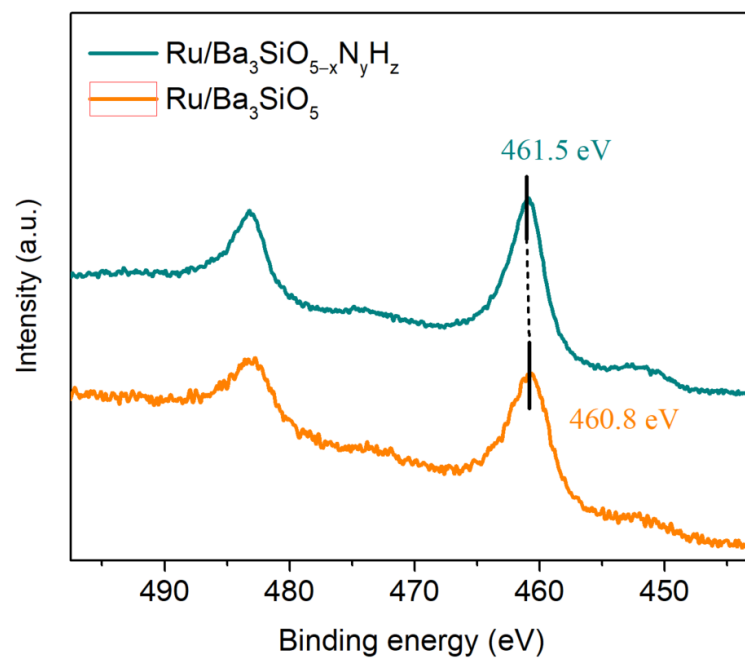
Supplementary Fig. 23. HAADF-STEM image of (a) Ru/ Ba₃SiO_{5-x}N_yH_z and (b) Ru/Ba₃SiO₅ collected after the ammonia synthesis test. Inset: particle size distribution of Ru nanoparticles.



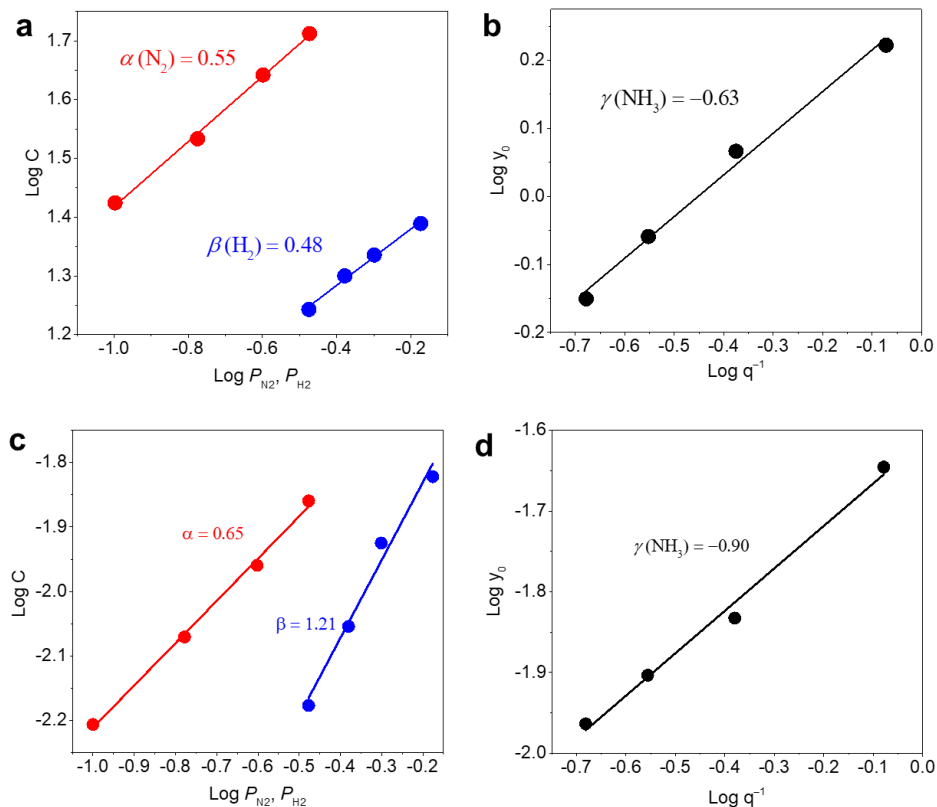
Supplementary Fig. 24. **a**, HAADF-STEM image and corresponding energy dispersive X-ray spectroscopy (EDX)-mapping of Ru/Ba₃SiO_{5-x}N_yH_z_HS collected after the ammonia synthesis test. **b**, Coverage mapping images of Si K, Ba L, and Ru L in panel **a**. **c**, HAADF-STEM image Ru/Ba₃SiO_{5-x}N_yH_z_HS collected after the ammonia synthesis. Inset: particle size distribution of Ru nanoparticles.



Supplementary Fig. 25. **a**, Ru K-edge X-ray absorption near edge structure (XANES) spectra of the used Ru/Ba₃SiO_{5-x}N_yH_z, along with RuO₂ and Ru_foil. **b**, Corresponding Ru K-edge FT-EXAFS spectra of the samples.

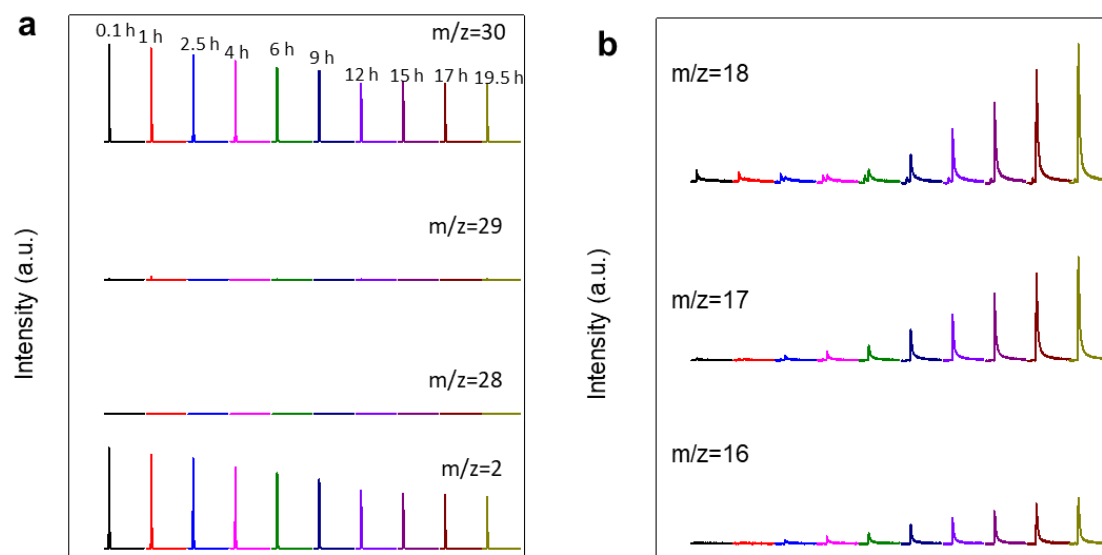


Supplementary Fig. 26. XPS Ru 3p spectra of used Ru/Ba₃SiO_{5-x}N_yH_z and Ru/Ba₃SiO₅.

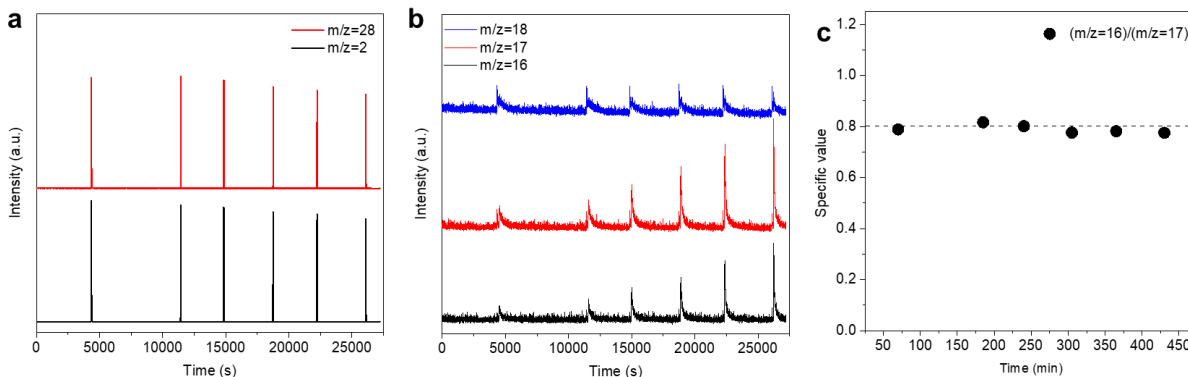


Supplementary Fig. 27. Dependence of NH_3 synthesis rate on the partial pressures of N_2 , H_2 and NH_3 over $\text{Ru}/\text{Ba}_3\text{SiO}_{5-x}\text{N}_y\text{H}_z$ at 340°C and 0.9 MPa (a, b) and $\text{Ba}_3\text{SiO}_{5-x}\text{N}_y\text{H}_z$ at 400°C and 0.9 MPa (c, d).

For the TM-free sample, the reaction order of N_2 is similar to that of Ru-loaded sample. However, its reaction orders of H_2 and NH_3 are more positive and more negative, respectively, than those for the Ru-loaded sample. This result suggests that NH_x species are more densely populated on $\text{Ba}_3\text{SiO}_{5-x}\text{N}_y\text{H}_z$ surface than hydrogen species, i.e., the hydrogenation processes are much difficult in the absence of Ru. On the other hand, the hydrogenation of surface nitrogen species is enhanced by the supported Ru particles, resulting in the high ammonia synthesis activity.

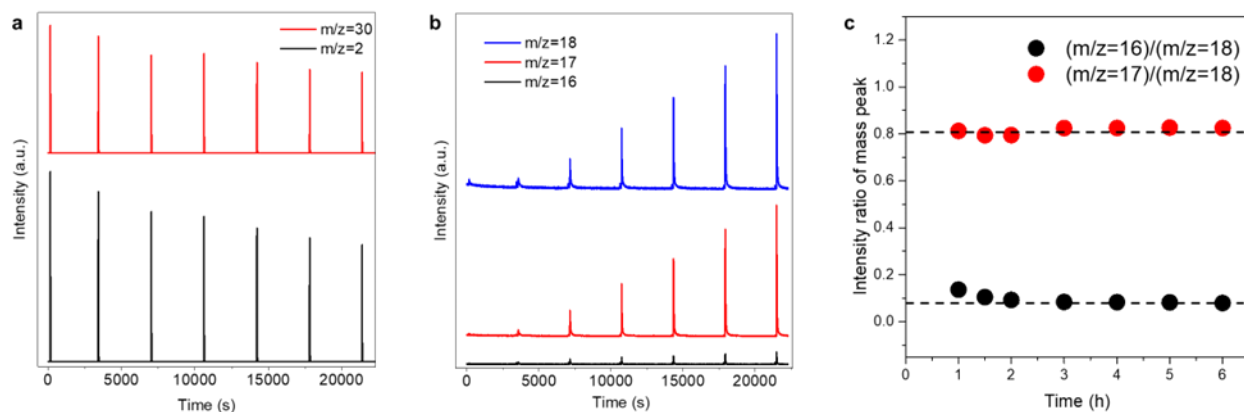


Supplementary Fig. 28. a, b, Mass spectra for ammonia synthesis from $^{15}\text{N}_2$ and H_2 over $\text{Ba}_3\text{SiO}_{5-x}\text{N}_y\text{H}_z$ at 400°C .

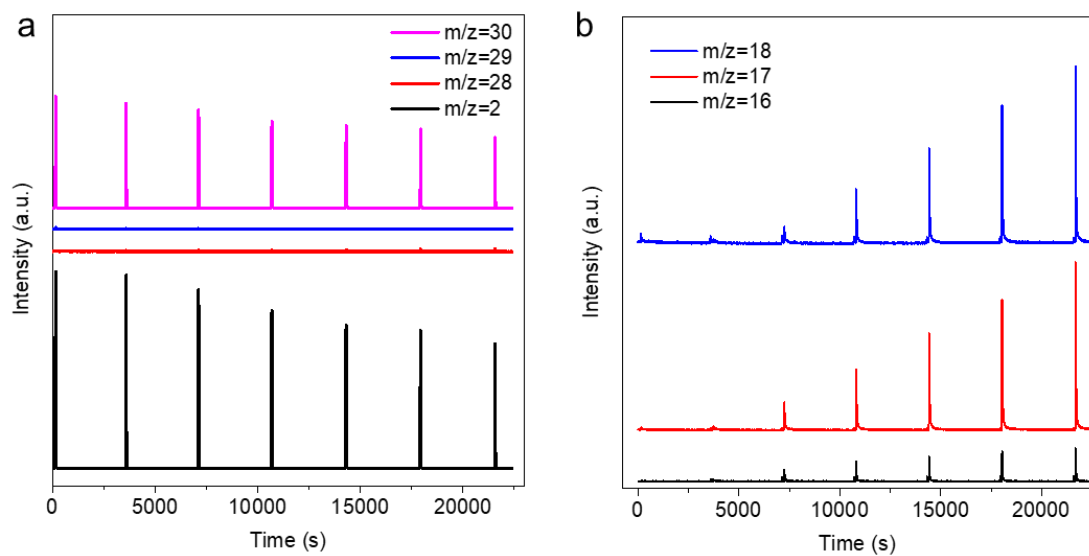


Supplementary Fig. 29. **a, b,** Mass spectra for ammonia synthesis from $^{14}\text{N}_2$ and H_2 over $\text{Ba}_3\text{SiO}_{5-x}\text{N}_y\text{H}_z$. **c,** Reaction time profiles for the ratio changes of 16/17 according to (**b**).

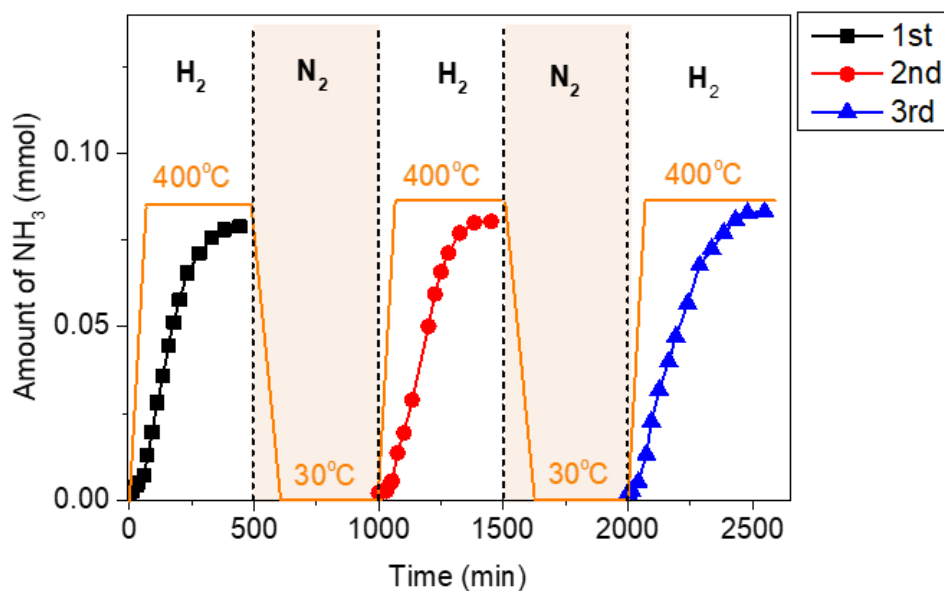
The $m/z=18$ (water) signal is due to the gas sampling system of closed glass circulation reactor. The gas in the sampling loop (pressure < 0.1 MPa) was flushed out with He gas (0.1 MPa) and injected into the GC and Q-mass. According to the pressure difference between the sampling loop and flushed gas, small amount of water from air atmosphere may be introduced to the injection line. However, the $m/z=18$ (water) signal does not increase with reaction time, which is contrast to the $m/z=17$ and 16 signals. In addition, the contribution of water to the mass signal intensity of $m/z=17$ is negligibly small compared with the theoretical mass signal ratio of $(m/z=17)/(m/z=18) = 0.21$ for H_2O . The observed mass signal ratio of $(m/z=16)/(m/z=17)$ is close to 0.8 corresponding to the theoretical ratio for NH_3 .



Supplementary Fig. 30. **a, b,** Mass spectra for ammonia synthesis from $^{15}\text{N}_2$ and H_2 over Ru/MgO at 400°C . **c,** Time courses for the intensity ratio of mass signal of $(m/z=16)/(m/z=18)$ and $(m/z=17)/(m/z=18)$ calculated based on panel b.

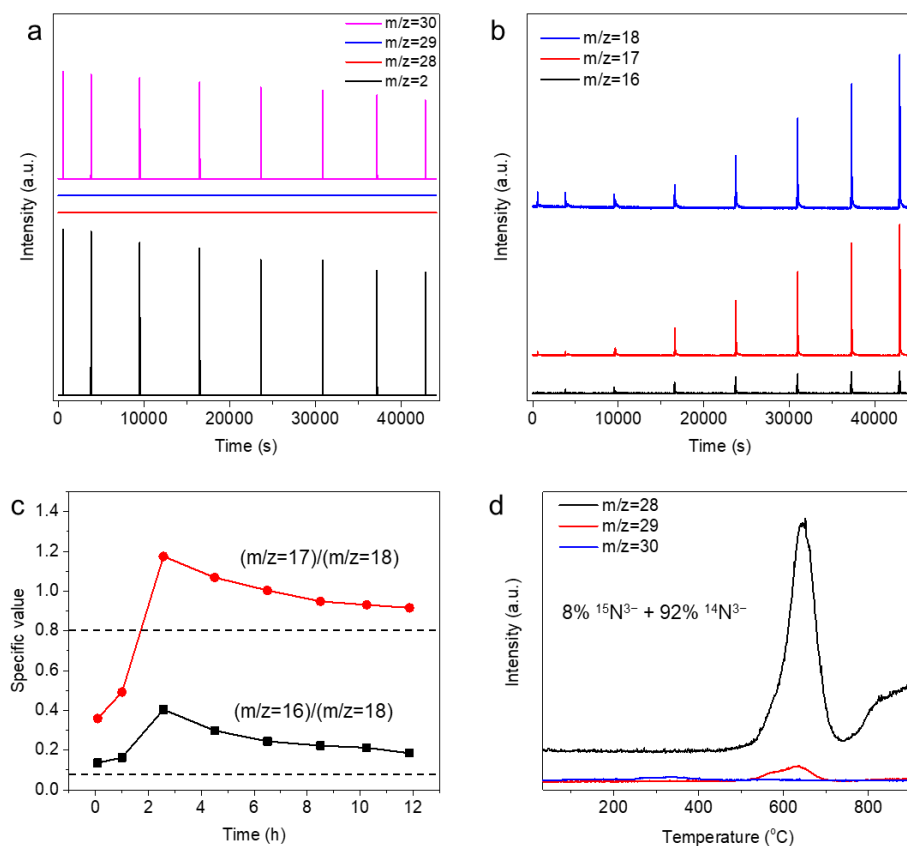


Supplementary Fig. 31. a, b, Mass spectra for ammonia synthesis from $^{15}\text{N}_2$ and H_2 over $\text{Ru}/\text{Ba}_3\text{SiO}_{5-x}\text{N}_y\text{H}_z$ at 400°C .

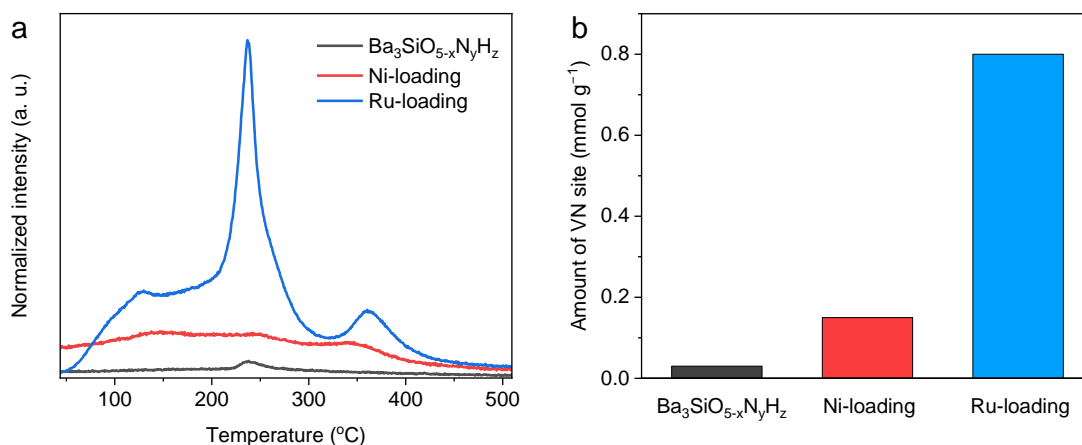


Supplementary Fig. 32. Ammonia formation over used $\text{Ru/Ba}_3\text{SiO}_{5-x}\text{N}_y\text{H}_z$ (0.1 g) under pure flow of pure H_2 (45 mL min^{-1}) and pure N_2 (15 mL min^{-1}) at 0.1 MPa (The orange line indicates the heating program).

The $\text{Ru/Ba}_3\text{SiO}_{5-x}\text{N}_y\text{H}_z$ sample was heated under pure H_2 flow from 30 to 400°C and kept at 400°C for several hours. Then, the reaction gas was switched to pure N_2 and naturally cooling to 30°C . This reaction cycle was repeated several times. The ammonia formation during the catalytic cycle is monitored by ion-chromatography. From this experiment, it was found that N_2 molecule can be captured at V_a site at room temperature, and then hydrogenated to form NH_3 at elevated temperature. Furthermore, the amount of the adsorbed N_2 molecules at V_a sites can be quantitatively monitored by the ammonia production via hydrogenation by H_2 .

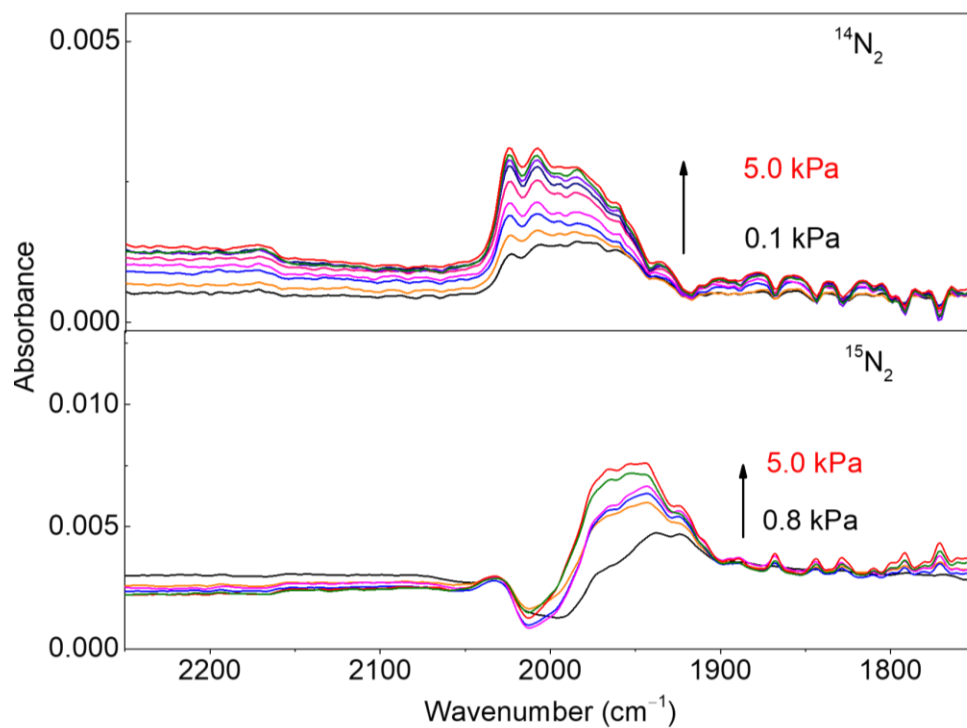


Supplementary Fig. 33. **a, b**, Mass spectra for ammonia synthesis from $^{15}\text{N}_2$ and H_2 over $\text{Ni}/\text{Ba}_3\text{SiO}_{5-x}\text{N}_y\text{H}_z$ at 400°C **c**, Time courses for the intensity ratio of mass signals of $(m/z=16)/(m/z=18)$ and $(m/z=17)/(m/z=18)$. **d**, TPD analysis of the sample collected after the isotope labeled ammonia synthesis.



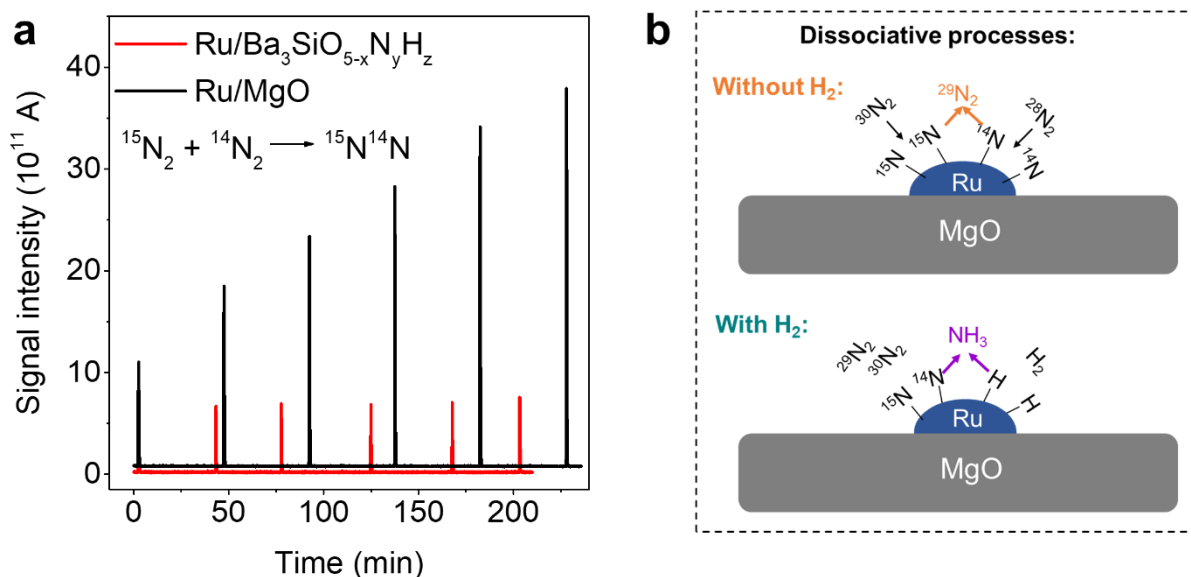
Supplementary Fig. 34. (a) NH_3 desorption ($m/z=17$) profiles during H_2 -TPR from $\text{Ba}_3\text{SiO}_{5-x}\text{N}_y\text{H}_z$, $\text{Ba}_3\text{SiO}_{5-x}\text{N}_y\text{H}_z$ (Ni-loading), and $\text{Ba}_3\text{SiO}_{5-x}\text{N}_y\text{H}_z$ (Ru-loading). All the above samples are collected after ammonia synthesis test. The TMs loading amount are both 1.5 wt.%.

Ammonia was formed upon heating the as-prepared $\text{Ba}_3\text{SiO}_{5-x}\text{N}_y\text{H}_z$ under a flow of $\text{H}_2(5\%)/\text{Ar}(95\%)$ (H_2 -TPR), which means that N^{3-} on the surface of $\text{Ba}_3\text{SiO}_{5-x}\text{N}_y\text{H}_z$ is hydrogenated to ammonia. Upon Ru-loading, the amount of ammonia production was 24 times higher than that of bare $\text{Ba}_3\text{SiO}_{5-x}\text{N}_y\text{H}_z$. The resultant V_N density is, thus, estimated to be 0.80, 0.15, and 0.03 mmol g^{-1} for Ru-loaded, Ni-loaded, and TM-free $\text{Ba}_3\text{SiO}_{5-x}\text{N}_y\text{H}_z$ samples, respectively. While the estimated V_N density is not necessarily the same as that under ammonia synthesis conditions, the above results clearly indicate that TM-loading significantly promotes nitrogen vacancy formation on the $\text{Ba}_3\text{SiO}_{5-x}\text{N}_y\text{H}_z$ under the ammonia synthesis conditions. And the strong Ru-N interaction facilitates the V_N formation rather than Ni-N interaction.

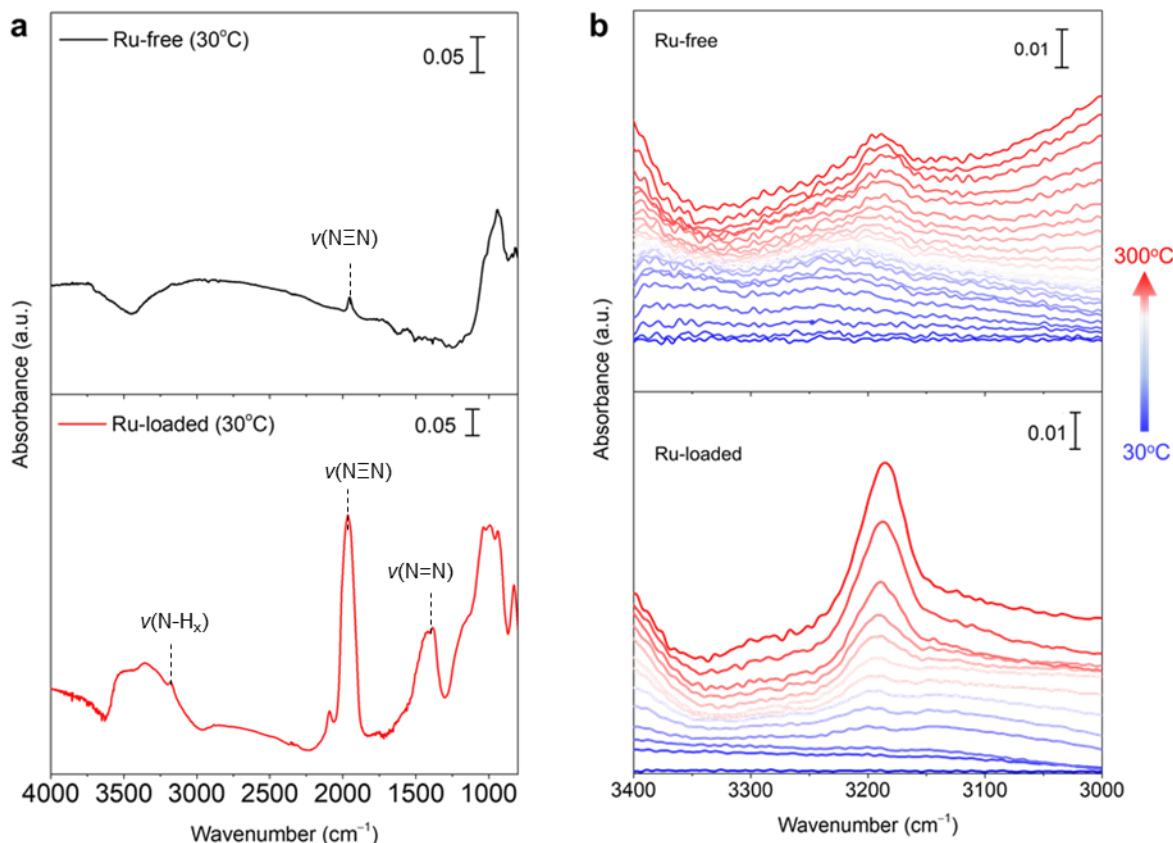


Supplementary Fig. 35. DRIFTS N_2 adsorption on $\text{Ba}_3\text{SiO}_{5-x}\text{N}_y\text{H}_z$ at -170°C under various pressures of $^{14}\text{N}_2$ or $^{15}\text{N}_2$.

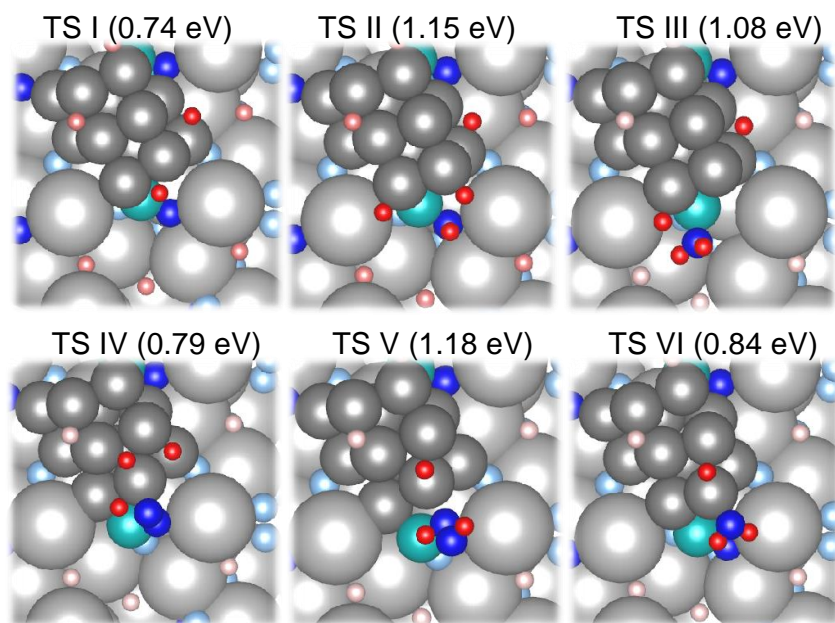
The N_2 peak intensity increased with the N_2 pressure and the peak position showed a red-shift of $60\text{--}70\text{ cm}^{-1}$ when $^{14}\text{N}_2$ was replaced by $^{15}\text{N}_2$. This isotope effect is clear evidence that the observed peaks are attributed to chemisorbed N_2 on $\text{Ba}_3\text{SiO}_{5-x}\text{N}_y\text{H}_z$ with end-on geometry.



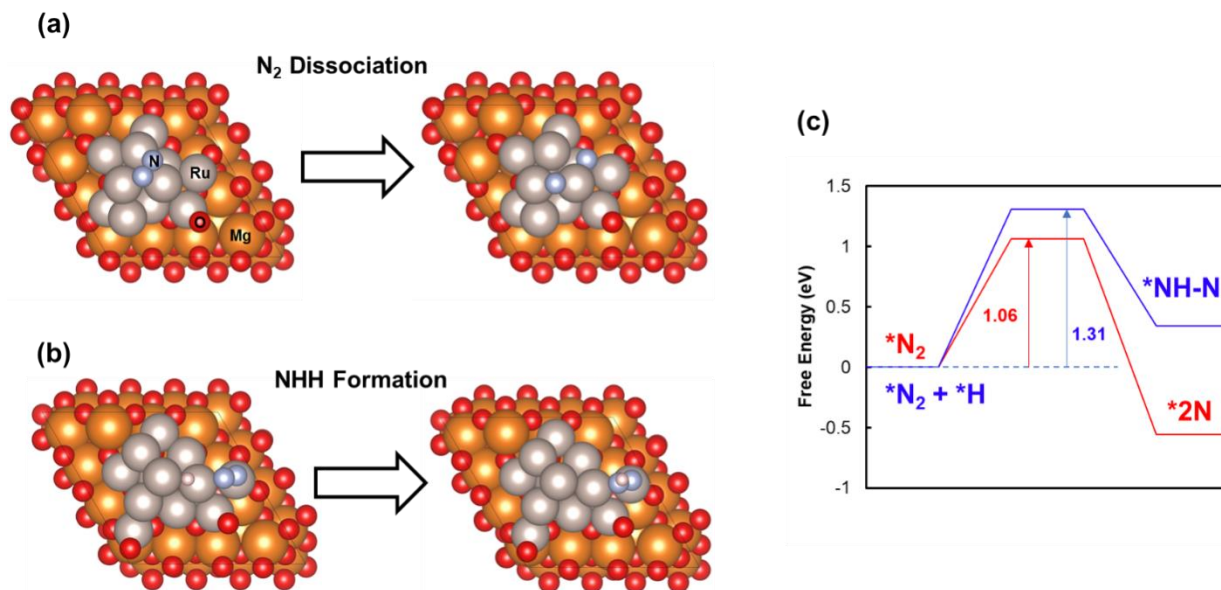
Supplementary Fig. 36. (a) Time courses for mass signal of $m/z=29$ during isotope N_2 exchange measurement for Ru/Ba₃SiO_{5-x}H_yN_z and Ru/MgO from $^{15}\text{N}_2$ (4 kPa) and $^{14}\text{N}_2$ (16 kPa) at 400 °C. (b) Schematic illustration of the dissociative ammonia synthesis processes over conventional Ru/MgO catalyst.



Supplementary Fig. 37. a, DRIFTS of $\text{Ba}_3\text{SiO}_{5-x}\text{N}_y\text{H}_z$ (Ru-free) and $\text{Ru}/\text{Ba}_3\text{SiO}_{5-x}\text{N}_y\text{H}_z$ (Ru-loaded) under a flow of N_2 (3 mL min^{-1}) and H_2 (9 mL min^{-1}) at 30°C . **b**, *In situ* DRIFTS observation of intermediates formation on $\text{Ba}_3\text{SiO}_{5-x}\text{N}_y\text{H}_z$ (Ru-free) and $\text{Ru}/\text{Ba}_3\text{SiO}_{5-x}\text{N}_y\text{H}_z$ (Ru-loaded) under a flow of N_2 (3 mL min^{-1}) and H_2 (9 mL min^{-1}) at different temperatures range from 30 to 300°C . The spectra measured at 30°C in panel a were used as background for *In situ* DRIFTS measurements in Fig. 4d and Supplementary Fig. 37b. N_2 adsorption is observed for each sample at 30°C . The $\text{Ba}_3\text{SiO}_{5-x}\text{N}_y\text{H}_z$ sample was pretreated at $650^\circ\text{C}/\text{Ar}$ for 2h before *in situ* DRIFTS measurement. The $\text{Ru}/\text{Ba}_3\text{SiO}_{5-x}\text{N}_y\text{H}_z$ sample was pretreated at 400°C under ammonia synthesis condition.

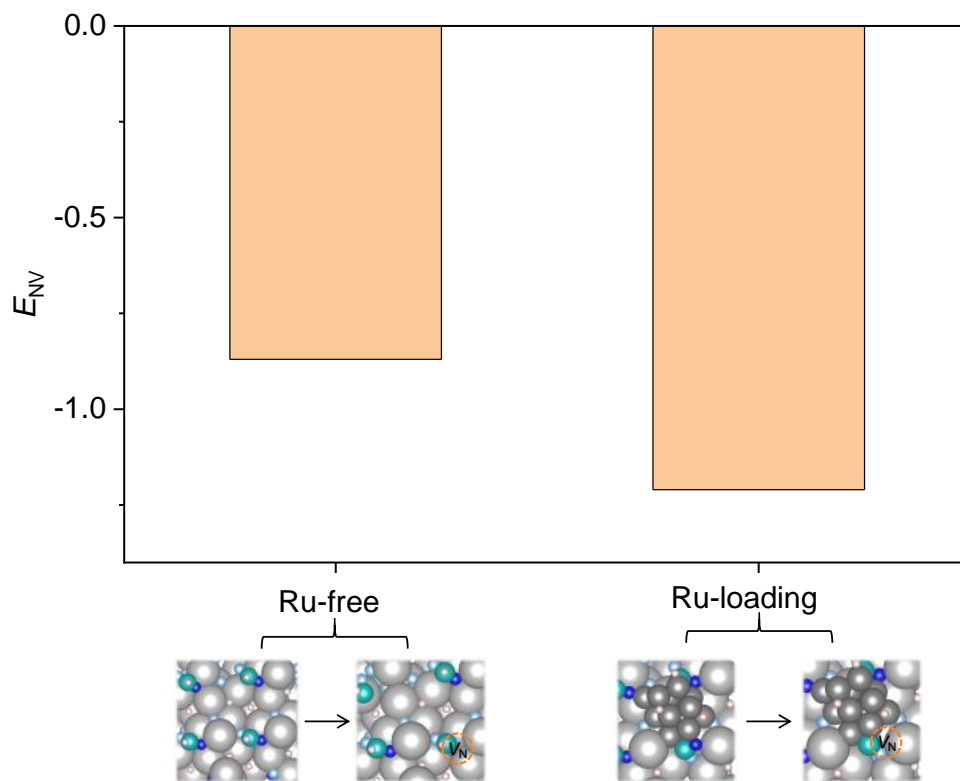


Supplementary Fig. 38. The structures of the transition states (TS I – TS VI) of Fig. 5. The energy barrier for each step is represented in parentheses.



Supplementary Fig. 39. Schematic illustration of **(a)** N_2 dissociation and **(b)** NNH formation on Ru/MgO and **(c)** corresponding energy diagrams.

The energy barrier for N_2 dissociation (1.06 eV) is lower than that for NNH formation (1.31 eV). The latter reaction is endothermic and the NNH* species is energetically unstable. Therefore, it makes sense that direct N_2 dissociation proceeds on Ru/MgO, and this is in good agreement with the conventional reaction mechanism on Ru surface.



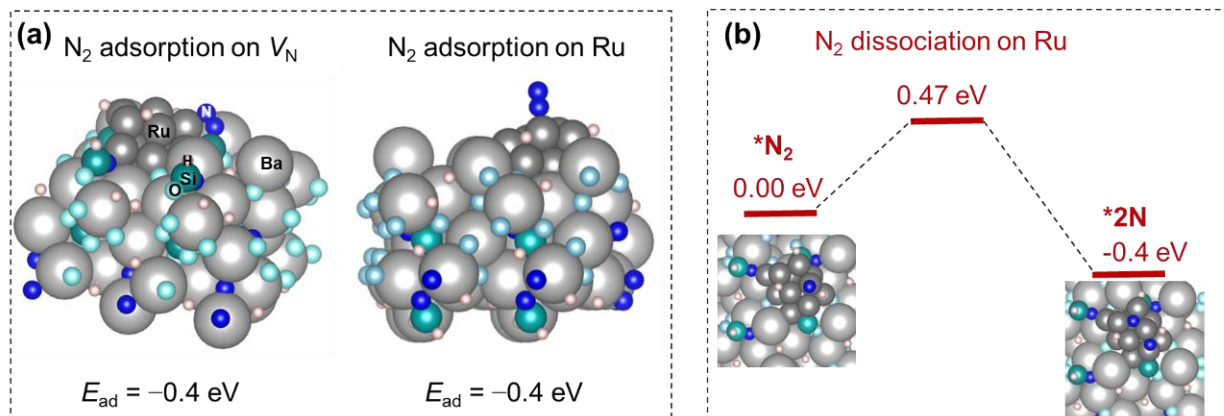
Supplementary Fig. 40. The formation energy of N vacancies (E_{NV}) on the $Ba_3SiO_{5-x}N_yH_z$ surface with and without Ru.

During ammonia synthesis reaction, N vacancy sites will be formed via the following reaction:
 $[Ba_3SiO_{5-x}N_yH_z + 3/2 H_2 (gas) \rightarrow Ba_3SiO_{5-x}N_yH_z\text{-with N-vacancy} + NH_3 (gas)]$.

Therefore, E_{NV} was defined as:

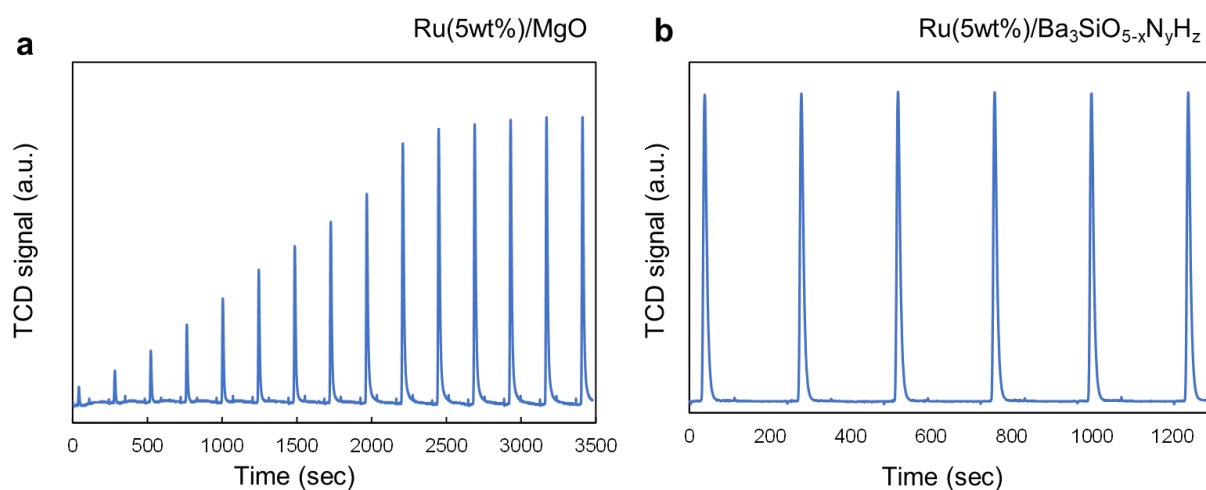
$$E_{NV} = \{E_{tot}(V_N/surface) + E_{tot}(NH_3)\} - \{E_{tot}(surface) + 1.5E_{tot}(H_2)\}$$

where $E_{tot}(V_N/surface)$ and $E_{tot}(surface)$ are the total energy for the optimized surface with and without N vacancies, respectively, and $E_{tot}(NH_3)$ and $E_{tot}(H_2)$ are the total energy of an NH_3 and H_2 molecule, respectively.



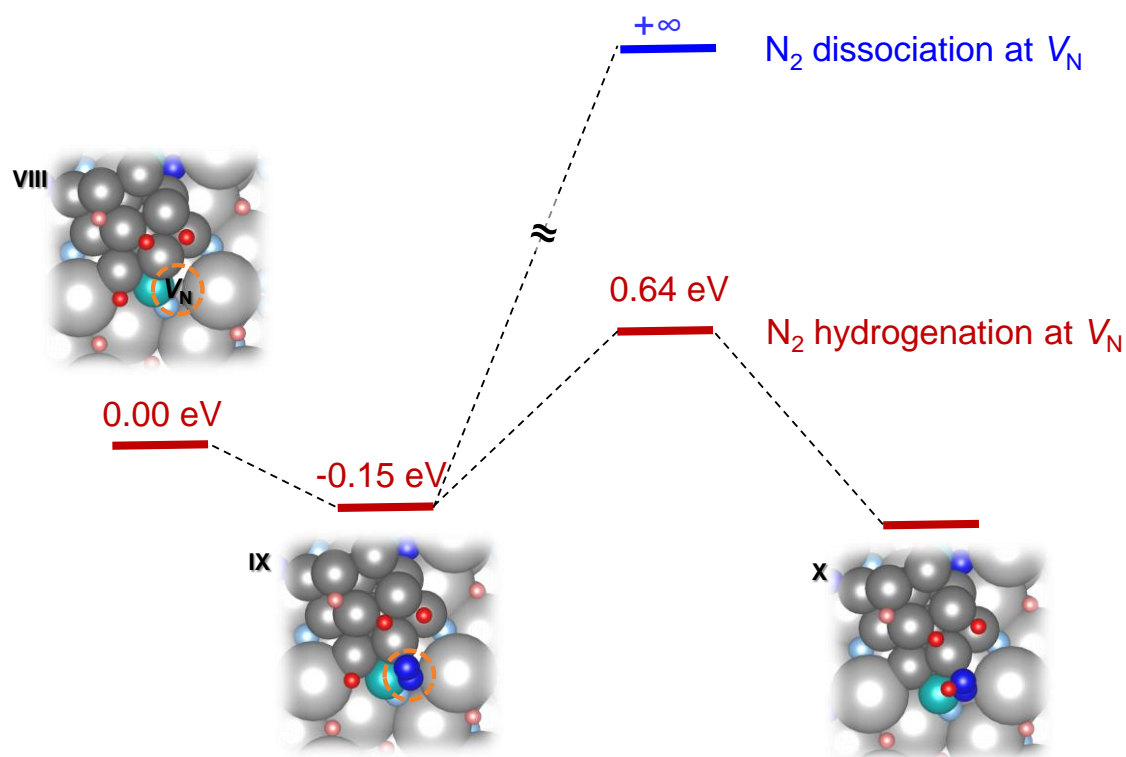
Supplementary Fig. 41. **a**, N_2 adsorption on the V_N site and Ru surface of $Ru/Ba_3SiO_{5-x}N_yH_z$. **b**, N_2 dissociation on Ru surface of $Ru/Ba_3SiO_{5-x}N_yH_z$.

N_2 adsorption on $Ru/Ba_3SiO_{5-x}N_yH_z$ was simulated without any adsorption from gas-phase H_2 . The hydrogen species on Ru was migrated from the lattice of $Ba_3SiO_{5-x}N_yH_z$ just after Ru cluster is loaded on $Ba_3SiO_{5-x}N_yH_z$ surface.



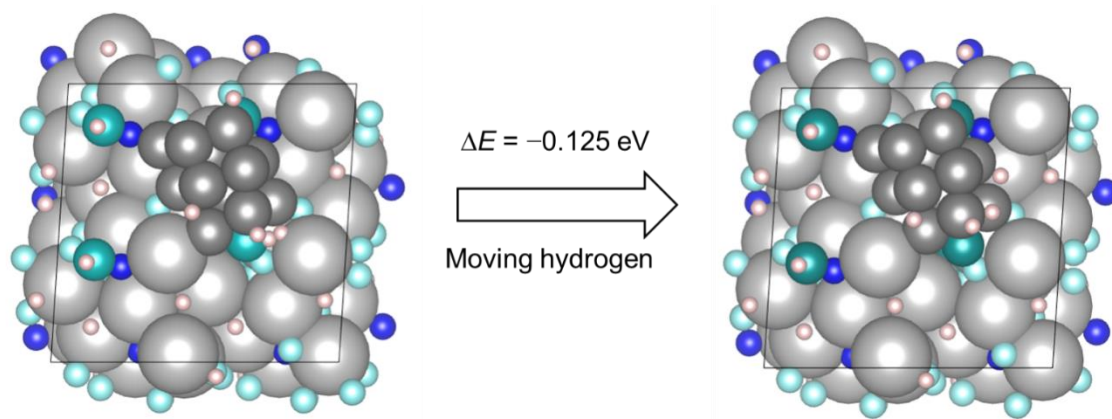
Supplementary Fig. 42. CO chemisorption on the used Ru/MgO (a) and Ru/Ba₃SiO_{5-x}N_yH_z catalyst (b) by the pulse method.

The amounts of CO adsorbed on Ru/MgO and Ru/Ba₃SiO_{5-x}N_yH_z were 125.2 $\mu\text{mol g}^{-1}$ and 0.60 $\mu\text{mol g}^{-1}$, respectively. Assuming that the CO/Ru adsorption ratio is 1, the mean Ru particle size of each catalyst was determined to be 4.8 nm and 436.1 nm, respectively. This result clearly indicates that Ru metal surface is barely exposed on Ru/Ba₃SiO_{5-x}N_yH_z since it is covered by the support components.

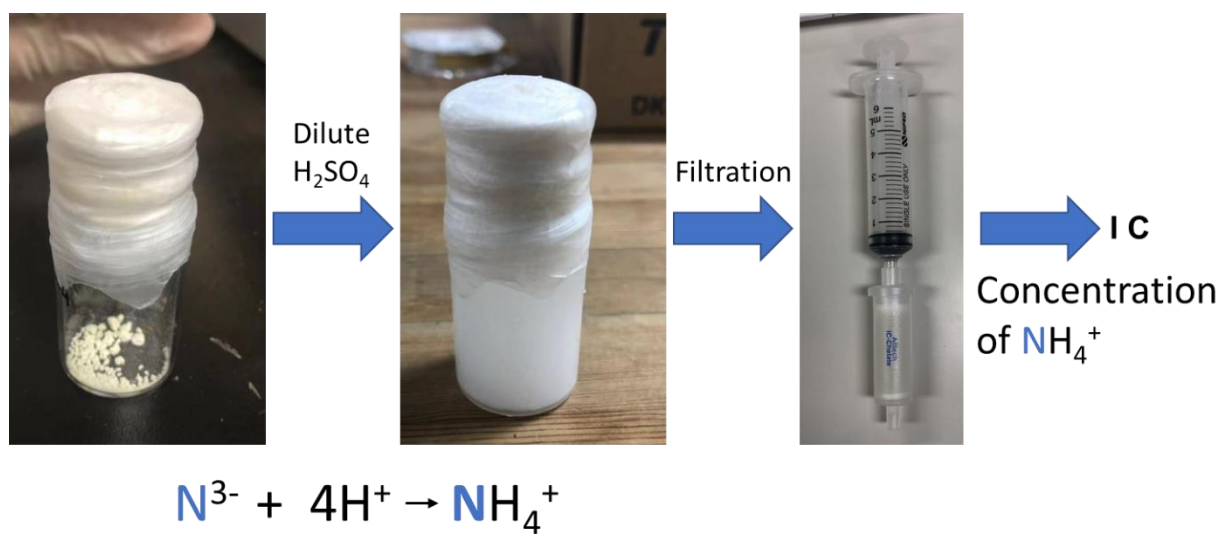


Supplementary Fig. 43. N_2 activation via the dissociative pathway (blue) and the associative pathway (red).

The energy barrier for N_2 dissociation at V_N site is extremely large, and therefore, the simulation for this step does not converge.



Supplementary Fig. 44. Hydrogen transfer during H_2 adsorption on the V_N site of $\text{Ru/Ba}_3\text{SiO}_{5-x}\text{N}_y\text{H}_z$.



Supplementary Fig. 45. Determination of the concentration of lattice N^{3-} in $\text{Ba}_3\text{SiO}_{5-x}\text{N}_y\text{H}_z$ by an acid dissolution method accompanied with ion chromatography (IC).

Supplementary Table 1. Lattice parameters and band gap of Ba_3SiO_5 , $\text{Ba}_3\text{SiO}_{2.87}\text{N}_{0.8}\text{H}_{1.86}$, and calculated $\text{Ba}_3\text{SiO}_{2.5}\text{NH}_2$.

Sample	a (Å)	c (Å)	V (Å ³)	$\Delta V/V_0^*$	E_g (eV)
Ba_3SiO_5 (Exp.)	7.308(1)	11.222(2)	599.4(2)	+0%	3.7
$\text{Ba}_3\text{SiO}_{2.87}\text{N}_{0.8}\text{H}_{1.86}$ (Exp.)	7.463(3)	11.724(5)	653.0 (6)	+8.9%	3.4
Ba_3SiO_5 (Cal.)	7.406	11.373	624.3	+0%	3.5
$\text{Ba}_3\text{SiO}_{2.5}\text{NH}_2$ (Cal.)	7.559	11.981	682.9	+9.4%	2.8

* $\Delta V/V_0$ means the cell volume expansion from Ba_3SiO_5 (Exp.) to $\text{Ba}_3\text{SiO}_{2.87}\text{N}_{0.8}\text{H}_{1.86}$ (Exp.), or Ba_3SiO_5 (Cal.) to $\text{Ba}_3\text{SiO}_{2.5}\text{NH}_2$ (Cal.).

Supplementary Table 2. DFT calculation of N-H pair at O-O pair ($\text{Ba}_3\text{SiO}_{5-2x}\text{N}_x\text{H}_x$).

x	substituted sites	$\Delta H_f(\text{eV})$	$V (\text{\AA}^3)$		$E_g (\text{eV})$
2.50	16 O1 + 4 O2		654.65	+4.9%	0.24
2.00	16 O1	-196.0	648.96	+4.0%	1.62
2.00	14 O1 + 2 O2	-195.9	655.54	+5.0%	1.76
2.00	12 O1 + 4 O2	-195.8	652.91	+4.6%	0.37
1.50	12 O1	-208.5	649.52	+4.0%	1.54
1.50	10 O1 + 2 O2	-208.4	658.11	+5.4%	1.19
1.50	8 O1 + 4 O2	-208.2	645.12	+3.3%	0.98
1.00	8 O1	-221.0	640.91	+2.7%	2.61
1.00	6 O1 + 2 O2	-220.9	654.70	+4.9%	2.20
1.00	4 O1 + 4 O2	-220.6	643.02	+3.0%	0.32
0.50	4 O1	-233.6	632.13	+1.3%	2.86
0.50	4 O2	-233.7	636.22	+1.9%	2.19
0.00			624.28		3.49

For the computation models of $\text{Ba}_3\text{SiO}_{5-2x}\text{N}_x\text{H}_x$ (N-H pairs that substitute two O sites ($2\text{O}^{2-} \Rightarrow \text{N}^{3-} + \text{H}^+$)), the energy is decreased with the decrease of amount of N-H pairs that substitute different oxygen sites. Although the energy of the model $\text{Ba}_3\text{SiO}_{5-2x}\text{N}_x\text{H}_x$ with $x=0.5$ ($\text{Ba}_3\text{SiO}_4\text{N}_{0.5}\text{H}_{0.5}$) and with N-H pairs substitute the O_2 sites is the smallest one. The lattice parameters and compositions is far from the experimental results.

Supplementary Table 3. DFT calculation of H-H pair at O ($\text{Ba}_3\text{SiO}_{5-y}\text{H}_{2y}$).

y	Substituted sites	ΔH_f (eV)	V (\AA^3)		E_g (eV)
1.00	4 O1	-233.6	672.25	+7.7%	3.11
	4 O2	-231.0	643.59	+3.1%	metal
0.50	2 O2		639.92	+2.5%	metal
0.00			624.28		3.49

Although the computation models of $\text{Ba}_3\text{SiO}_{5-y}\text{H}_{2y}$ (H-H pair replace oxygen, $\text{O}^{2-} \Rightarrow 2\text{H}^-$) shows a smaller energy, their compositions is far from the experimental results.

Supplementary Table 4. DFT calculation of N-H pair & H-H pair ($\text{Ba}_3\text{SiO}_{5-2x-y}\text{N}_x\text{H}_{x+2y}$).

x	Substituted sites	y	Substituted sites	$\Delta H_f(\text{eV})$	$V(\text{\AA}^3)$		$E_g(\text{eV})$
1.00	4 O1	0.25	1 O1	-218.0	654.18	+4.9%	2.95
1.00	4 O1	0.25	1 O2	-218.6	669.72	+7.3%	2.97
1.00	2 O1 + 2O2	0.25	1 O1	-	-	-	-
1.00	2 O1 + 2O2	0.25	1 O2	-218.5	666.15	+6.7%	2.21
1.00	4 O2	0.25	1 O1	-217.5	666.02	+6.7%	1.48
1.00	2 O1	0.50	2 O1	-215.3	653.86	+4.7%	3.01
1.00	2 O1	0.50	1 O1 + 1 O2	-216.1	683.18	+9.4%	3.06
1.00	2 O1	0.50	2 O2	-217.0	682.89	+9.4%	2.78
1.00	1 O1 + 1 O2	0.50	2 O1	-215.2	678.48	+8.7%	1.89
1.00	1 O1 + 1 O2	0.50	1 O1 + 1 O2	-215.7	695.91	+11.5%	2.11
1.00	1 O1 + 1 O2	0.50	2 O2	-216.6	670.86	+7.5%	2.23
1.00	2 O2	0.50	2 O1	-214.9	690.58	+10.6%	1.38
0.00		0.00			624.28		3.49

For the computation models of $\text{Ba}_3\text{SiO}_{5-2x-y}\text{N}_x\text{H}_{x+2y}$ (N-H pair replace O-O pair and with an extra H-H pair). An x value of 1.00 and y value of 0.50 could give a formula of $\text{Ba}_3\text{SiO}_{2.5}\text{NH}_2$ is mostly close to the experimental result. When fixed this compositions, the lowest energy of the computation model was found to be the case with 2O₁ sites substituted by N-H pair ($2\text{O}_1^{2-} \Rightarrow \text{N}^{3-} + \text{H}^+$) and one O₂ site was substituted by additional H-H pair ($\text{O}_2^{2-} \Rightarrow 2\text{H}^+$). In addition, the lattice expansion value ($\Delta V/V_0 = +9.4\%$) is very close to the experimental result (Supplementary Table 1). We therefore select this structure as the benchmarking computation model of $\text{Ba}_3\text{SiO}_{5-x}\text{N}_y\text{H}_z$.

Supplementary Table 5. Concentration of H^- and N^{3-} of $\text{Ba}_3\text{SiO}_{5-x}\text{N}_y\text{H}_z$ pretreated in different conditions.

Sample	N^{3-} contents (mmol g^{-1})	H^- contents (mmol g^{-1})
As-prepared $\text{Ba}_3\text{SiO}_{5-x}\text{N}_y\text{H}_z$	1.60 (± 0.03)	3.74 (± 0.19)
$\text{Ba}_3\text{SiO}_{5-x}\text{N}_y\text{H}_z$ Ar/650°C	1.48 (± 0.02)	0.60 (± 0.05)
$\text{Ba}_3\text{SiO}_{5-x}\text{N}_y\text{H}_z$ Ar/650°C-used	1.54 (± 0.03)	3.62 (± 0.20)
Ru/ $\text{Ba}_3\text{SiO}_{5-x}\text{N}_y\text{H}_z$ -used	1.56 (± 0.05)	3.12 (± 0.22)

N^{3-} and H^- content was determined by an acid dissolution method (Supplementary Fig. 41) and TPD, respectively.

Supplementary Table 6. ICP-AES analysis result of $\text{Ba}_3\text{SiO}_{5-x}\text{N}_y\text{H}_z$ collected after ammonia synthesis test.

Sample	Concentration (ppm)					
	Fe	Co	Ni	Mo	Ru	Ba
Blank	<0.01	<0.01	0.01	0.01	0.01	<0.01
$\text{Ba}_3\text{SiO}_{5-x}\text{N}_y\text{H}_z$ after reaction	<0.01	<0.01	0.01	0.01	0.01	90

Inductively coupled plasma atomic emission spectroscopy (ICP-AES) analysis of the $\text{Ba}_3\text{SiO}_{5-x}\text{N}_y\text{H}_z$ after the ammonia synthesis test show that possible impurities such as Fe, Co, Ni, Mo, and Ru are negligible low (below 0.01 ppm), which are almost identical to the blank level.

Supplementary Table 7. Summary of the catalytic ammonia synthesis performance at around 0.9 MPa and 300 °C for the most active Ru-based heterogeneous catalysts.

Catalyst	Ru content (wt.%)	r (mmol g _{cat} ⁻¹ h ⁻¹)	r (mmol g _{Ru} ⁻¹ h ⁻¹)	WHSV (mL g ⁻¹ h ⁻¹)	Ratio of H ₂ /N ₂	Ref.
Ru/Ba ₃ SiO _{5-x} N _y H _z	1.5	6.0	398	36000	3/1	This work
Ru/Ba ₃ SiO _{5-x} N _y H _z _HS	1.5	15.7	1047	36000	3/1	This work
Ru/Ba ₃ SiO _{5-x} N _y H _z _HS	1.5	25.1	1673	60000	3/2	This work
Ru/Ba ₃ SiO _{5-x} N _y H _z _HS	5.0	40.1 (1.0 MPa)	802	60000	3/2	This work
Ru/Ba-Ca(NH ₂) ₂	10	23.3	233	36000	3/1	23
Ba ₂ RuH ₆ /MgO	5	34.0 (1.0 MPa)	680 (1.0 MPa)	60000	2/3	15
Li ₄ RuH ₆ /MgO	8	22.0 (1.0 MPa)	275 (1.0 MPa)	60000	2/3	15
Ru/BaO-CaH ₂	10	16.5	165	36000	3/1	27
Ru/Ba/LaCeO _x	5	~15 (1.0 MPa)	~300	72000	3/1	28
Ru/Ca ₂ N:e ⁻	1.8	4.1 (320 °C)	228 (320 °C)	36000	3/1	29
Ru/C12A7:e ⁻	1.8	1.7 (320 °C)	94 (320 °C)	36000	3/1	12
Ru/BaCeO _{3-x} N _y H _z	4.5	5.0	111	36000	3/1	26